Understanding Micro- and Macro-Mechanics of Soil Liquefaction—A Necessary Step for Field-Scale Assessment

Thesis by
Utkarsh Mital

In Partial Fulfillment of the Requirements for the degree of
Doctor of Philosophy

CALIFORNIA INSTITUTE OF TECHNOLOGY
Pasadena, California

2016
Defended April 29, 2016

Utkarsh Mital
ORCID: 0000-0001-9794-382X

ACKNOWLEDGEMENTS

Firstly, I would like to express my sincere gratitude to my advisor Prof. José Andrade for the continuous support of my Ph.D. research, for his patience, motivation, and guidance. I could not have imagined having a better advisor and mentor for my Ph.D. research. Besides my advisor, I would like to thank the rest of my thesis committee—Prof. Nadia Lapusta, Prof. Domniki Asimaki, and Prof. Jean-Paul Ampuero—for their insightful comments, which helped widen my research from various perspectives. I also thank my lab-mates, for various stimulating discussions. In particular, I would like to thank Dr. Toktam Mohammadnejad and Reid Kawamoto, two of my lab-mates who were also my collaborators. Thanks must also go to Dr. Sergio Andres Galindo-Torres at University of Queensland, who was of great help during the initial period of my Ph.D. research.

I thank my friends, for being a support-system, and for all the fun we have had over the course of my Ph.D. I also thank the staff at the Mechanical and Civil Engineering department, as well as the staff at International Student Programs, who have been a helpful resource throughout my time at Caltech.

A special thanks goes to Brian Brophy and everyone associated with Caltech Theater. Theater has been a huge part of my life at Caltech, and has helped me in exploring my artistic side.

Last but not the least, I would like to thank my family—my parents and my sister—for being a constant pillar of support and encouragement throughout my life.

ABSTRACT

Liquefaction is a devastating instability associated with saturated, loose, and cohesionless soils. It poses a significant risk to distributed infrastructure systems that are vital for the security, economy, safety, health, and welfare of societies. In order to make our cities resilient to the effects of liquefaction, it is important to be able to identify areas that are most susceptible. Some of the prevalent methodologies employed to identify susceptible areas include conventional slope stability analysis and the use of so-called liquefaction charts. However, these methodologies have some limitations, which motivate our research objectives. In this dissertation, we investigate the mechanics of origin of liquefaction in a laboratory test using grain-scale simulations, which helps (i) understand why certain soils liquefy under certain conditions, and (ii) identify a necessary precursor for onset of flow liquefaction. Furthermore, we investigate the mechanics of liquefaction charts using a continuum plasticity model; this can help in modeling the surface hazards of liquefaction following an earthquake. Finally, we also investigate the microscopic definition of soil shear wave velocity, a soil property that is used as an index to quantify liquefaction resistance of soil. We show that anisotropy in fabric, or grain arrangement can be correlated with anisotropy in shear wave velocity. This has the potential to quantify the effects of sample disturbance when a soil specimen is extracted from the field. In conclusion, by developing a more fundamental understanding of soil liquefaction, this dissertation takes necessary steps for a more physical assessment of liquefaction susceptibility at the field-scale.

PUBLISHED CONTENT AND CONTRIBUTIONS

[1] U. Mital and J.E. Andrade. "Mechanics of origin of flow liquefaction instability under proportional strain triaxial compression". In: *Acta Geotechnica* (2016), pp. 1–11. DOI: 10.1007/s11440-015-0430-8. URL: http://link.springer.com/article/10.1007/s11440-015-0430-8/fulltext.html.
U. Mital participated in the conception of the project, developed the flow liquefaction potential definition, identified the necessary precursor for onset of flow liquefaction, ran the numerical simulations to obtain the data, and wrote the manuscript.

[2] U. Mital, R.Y. Kawamoto, and J.E. Andrade. "Effect of fabric on shear wave velocity in granular materials". submitted. 2016.
U. Mital participated in the conception of the project, developed the numerical experiment, ran the numerical simulations to obtain the data, and wrote the manuscript.

[3] U. Mital, T. Mohammadnejad, and J.E. Andrade. "Flow liquefaction instability as a mechanism for lower end of liquefaction charts". submitted. 2016.
U. Mital participated in the conception of the project, developed the hypothesis, ran the numerical simulations to obtain the data, and wrote the manuscript.

TABLE OF CONTENTS

LIST OF ILLUSTRATIONS

Number *Page*

LIST OF TABLES

Number *Page*

NOMENCLATURE

Consolidation coefficient K_0. Ratio of horizontal stresses to vertical stresses on a soil element.

Dense soil. Soil that tends to expand, or dilate under drained loading.

Drained loading. A condition that allows drainage of pore fluid when a soil assembly is loaded.

Effectuve stress. Stress borne only by the soil skeleton.

Loose soil. Soil that tends to compact under drained loading.

Pore pressure. Stress borne by the pore fluid.

Relative Density $\mathbf{D_R}$. $D_R = \dfrac{e_{max} - e}{e_{max} - e_{min}}$, where e_{max} is the maximum void ratio corresponding to a very loose state, e_{min} is the minimum void ratio corresponding to a very dense state, and e is the void ratio.

Total stress. Stress borne by the combined solid-fluid assembly.

Undrained loading. A condition that prevents drainage of pore fluid when a soil assembly is loaded.

Void ratio e. Ratio of volume of void space to volume of solids, in a soil assembly.

Chapter 1

INTRODUCTION

1.1 Introduction to Liquefaction

Liquefaction is a devastating instability associated with saturated, loose, and cohesionless soils. It is typically associated with earthquake-induced shaking that causes the ground to lose its bearing strength and act like a fluid. This can cause entire buildings to topple and cars to get sucked in. It can cause surface layers to slide downhill, damaging roads and rupturing distributed infrastructure systems like water and gas lines. It can also cause floatation, whereby objects buried underground such as pipelines and manhole covers float up to the surface. The 1964 earthquake in Niigata, Japan and the 2010-11 earthquake sequence in Christchurch, New Zealand provide prime examples of earthquake-induced liquefaction failures.

Although primarily associated with earthquakes, liquefaction can also occur under static loading conditions [44]. Static liquefaction has been observed as a cause for failure of slopes in hydraulic fill dams, spoil tips, and tailings [8]. Examples include the 1966 Aberfan disaster, which resulted in the loss of 144 lives, and the failure of the Fort Peck Dam in 1936 that led to the loss of 80 lives. More recently, in November 2015, the failure of the Fundao dam in Brazil that resulted in the death of 19 people is also suspected to be caused by liquefaction [43].

Liquefaction is typically characterized by generation of excess pore pressure under undrained loading. The tendency of loose sands to densify under drained loading is well known [44]. When loose sands are saturated and loaded under undrained conditions, the tendency to densify causes an increase in pore pressure, leading to a decrease in effective confining pressure. This lowers the shear strength of the soil, causing it to liquefy. Based on the mechanism of deformation, liquefaction can be divided into flow liquefaction and cyclic mobility. Flow liquefaction can occur when the shear stress required for static equilibrium of a soil mass is greater than the shear strength of the soil in its liquefied state. It can occur under both static and cyclic loading. Once triggered, the soil experiences large deformations which may seem sudden and are catastrophic. Cyclic mobility, on the other hand, can occur when the shear stress required for static equilibrium of a soil mass is less than the shear strength of soil. It can occur only under cyclic loading. In contrast with flow liquefaction, cyclic mobility causes deformations to develop incrementally during an earthquake, and can lead to large permanent deformations that are termed 'lateral spreading' [44]. Chapter 3 discusses these mechanisms in greater detail.

1.2 Evaluation of liquefaction susceptibility

In order to mitigate the effects of liquefaction, it is important to be able to evaluate liquefaction susceptibility of a soil. This evaluation essentially consists of determining two kinds of stresses:

(a) Stresses imposed on the soil by external loading.

(b) Stresses needed to liquefy the soil.

If (a) ≥ (b), soil liquefies, else it is stable. Evaluation of stresses in (a) is based on a knowledge and estimation of field conditions. For instance, in the case of static slope stability analyses, the angle of the slope can be used as a metric to estimate imposed stresses [32, 48]. In the case of earthquake-induced loading, the so-called 'simplified procedure' is commonly used [34, 71, 88].

Evaluation of stresses in (b) can be achieved via laboratory or in-situ testing of soils. For slope stability analyses in the case of spoil tips, tailings, and hydraulic-fill dams, estimating stresses needed for soil liquefaction is often done by obtaining a soil sample from the site, and subjecting it to static compression in a laboratory test [32, 48]. For earthquake-induced liquefaction assessments, recourse is often sought to in-situ tests such as standard penetration tests, cone penetration tests, and shear velocity measurements [34, 88]. In-situ tests are considered more representative of field behavior than laboratory testing, since retrieval of soil specimens from the field using typical drilling and sampling techniques induces a lot of disturbance, which destroys the existing mechanical structure. This makes it difficult to translate laboratory test results onto field conditions [34, 88]. However, interpretation of in-situ tests often relies on empirical correlations [34, 88], which inherently restricts the scope of their application.

To help with the flow of this thesis, the next few sub-sections provide a brief review of (i) the triaxial compression test, which is a common laboratory test, and (ii) liquefaction charts, which are used to evaluate liquefaction resistance of soil to earthquakes. A review of these topics will help in motivating the research presented in this thesis.

(i) The Triaxial Compression Test

For slope stability analysis under static loading, estimating stresses needed for soil liquefaction is often done by subjecting a soil sample obtained from the site to static loading in a triaxial compression test [32, 48]. Subjecting a loose sand to triaxial compression under undrained loading causes it to liquefy; this is perhaps the simplest manifestation of liquefaction. The triaxial test involves using a cylindrical specimen, generally having a length/diameter ratio of 2, that is stressed under conditions of axial symmetry. Figure 1.1 shows a schematic of the test. A detailed description of the test setup can be found in a soil mechanics textbook [16, 85]. In essence, the soil specimen is confined in a rubber membrane, and is placed on a porous disc on a pedestal. There is a loading cap on top of the specimen that can impose an axial stress σ_a. The specimen is subjected to an all-round fluid pressure σ_r. There is also a provision for drainage of pore water through the pedestal that can also be used for measurement of pore water pressure if drainage is prevented.

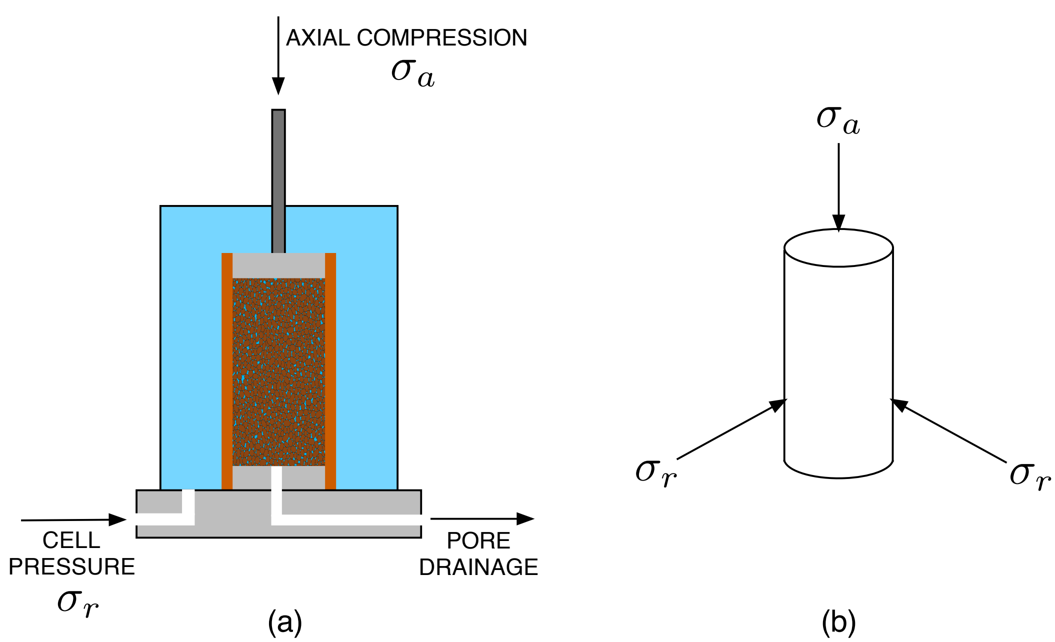

Figure 1.1: (a): Schematic diagram of the conventional triaxial test. (b): Imposed stress states

For the purpose of liquefaction testing, the specimen is first subjected to isotropic consolidation under drained conditions. Thereafter, it is subjected to axial compression under undrained conditions. Figure 1.2 shows the stress paths obtained during static triaxial compression tests of loose and dense sands, under undrained conditions. Note that $q = (\sigma_a - \sigma_r)$ is the deviatoric stress, $p = (\sigma_a + 2\sigma_r)/3$ is the total volumetric stress, and p' is the effective volumetric stress. Total stresses are the stresses borne by the solid-fluid assembly, while effective stresses are the stresses borne only by the soil skeleton. Total and effective deviatoric stresses are the same, since the interstitial fluid is assumed to be incapable of providing shearing resistance.

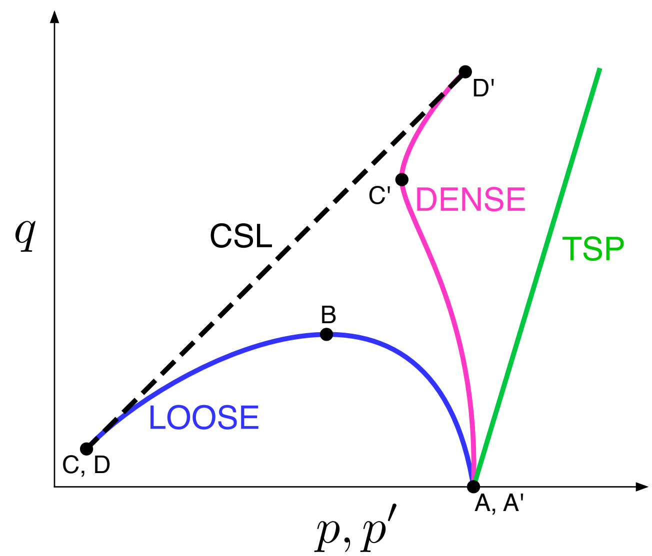

Figure 1.2: Effective stress paths of loose and dense sands under undrained triaxial compression. The total stress path (TSP) and critical state line (CSL) are also sketched for reference. A = start, B = Instability in loose sand, C & C' = phase transformation, D & D' = critical state. In loose sands, points C and D are often indistinguishable [36].

In the case of loose sands, the specimen undergoes a peak in stress space followed by a sudden collapse, accompanied by a large pore water pressure build up and extensive strain-softening. The peak in stress space is said to denote the onset of flow liquefaction instability [44]. On the other hand, dense sands are known to display a reversal in behavior - from contractive to dilative, during a phenomenon called 'phase transformation'. This phenomenon ostensibly provides stability to dense sands, whereby the pore water pressure build-up and strain softening are kept in check.

Conventionally, for static **slope stability analysis** under drained conditions, the stress state corresponding to the residual strength (or critical state) of the sand under drained loading is used as a measure of soil shear strength. For resistance to liquefaction, however, it has been suggested that the stress state corresponding to the peak (point B in Figure 1.2) in an undrained triaxial compression test should be used instead [32, 48]. Using analytical techniques like the 'method of slices' [16], or more advanced numerical techniques [28], the shear stress imposed on the soil can be calculated and compared with the soil strength to estimate a factor-of-safety.

(ii) Liquefaction charts

In order to evaluate liquefaction resistance of soils under dynamic or earthquake-induced loading, engineers often resort to liquefaction charts. Development of these charts involve (a) estimating stresses induced by an earthquake, and (b) estimating the strength of soils.

(a) Estimating stresses induced by an earthquake

Estimation of seismic demand on a soil element can be made via the 'simplified procedure', proposed by Seed and Idriss [71]. It is assumed that the seismic shear stresses induced at any depth in a soil deposit with a level ground surface are primarily due to the vertical propagation of horizontal shear waves. If the soil column above a soil element at depth h acted like a rigid body and the maximum ground surface acceleration were $a_{\max}$, the maximum shear stress $(\tau_{\max})_r$ on the soil element would be:

$$(\tau_{\max})_r = \frac{\gamma h}{g} a_{\max} = \sigma_v \frac{a_{\max}}{g} \tag{1.1}$$

where γ is the unit weight of the soil, and σ_v is the total vertical stress at depth h. See Figure 1.3. However, the soil column behaves like a deformable body, so the actual maximum shear stress $\tau_{\max}$ on the soil element would be:

$$\tau_{\max} = r_d (\tau_{\max})_r \tag{1.2}$$

where $r_d < 1$ is a stress reduction coefficient. $r_d = 1$ at the surface and decreases as the depth increases. Semi-empirical expressions exist for evaluating r_d up to a depth of 20 m [34, 88].

The cyclic stresses induced during an earthquake constitute an irregular time series with numerous cycles of different magnitudes. Studies have shown that an irregular

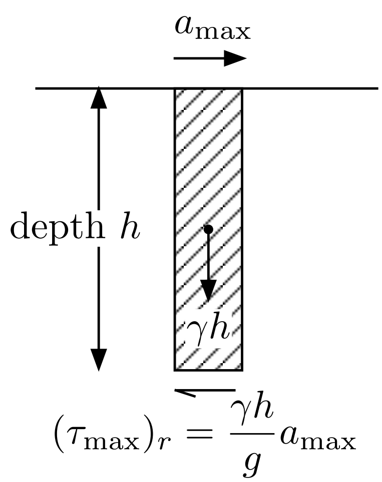

Figure 1.3: Maximum shear stress $(\tau_{\max})_r$ on a rigid block of sand at depth h from the surface.

time series can be approximated by a uniform cyclic stress time series with an equivalent number of uniform cycles [34, 70]. Seed and Idriss [71] arbitrarily chose a uniform average cyclic stress, τ_{avg} equal to 0.65 of the peak cyclic stress, $\tau_{\max}$. Hence:

$$\tau_{\text{avg}} = 0.65\,\sigma_v \frac{a_{\max}}{g} r_d \tag{1.3}$$

The number of uniform cycles N corresponding to τ_{avg} is semi-empirically related to earthquake magnitude [34, 70]. For instance, a magnitude 7.5 earthquake has been proposed to correspond to 15 cycles. The average cyclic stress is then normalized by the effective vertical confining pressure σ'_v to yield the cyclic stress ratio (CSR) imposed on a soil element at depth h by an earthquake:

$$\text{CSR} = \frac{\tau_{\text{avg}}}{\sigma'_v} = 0.65\,\frac{\sigma_v}{\sigma'_v}\frac{a_{\max}}{g} r_d \tag{1.4}$$

The seismic demand on a soil element is commonly expressed in terms of CSR. The CSR that is just sufficient to cause soil liquefaction is called the cyclic resistance ratio (CRR), and is a measure of the strength of soils. Determination of CRR is briefly reviewed next.

(b) Estimating strength of soils

Determination of in-situ CRR of sands can be done via laboratory testing of field samples [72]. The sample would be subjected to N cycles of cyclic loading, where N is empirically related to the earthquake magnitude. The uniform stress ratio (τ/σ'_v) that would cause liquefaction in N cycles would be recorded as CRR, and then checked against CSR obtained in equation 1.4. If CRR exceeds CSR, the soil is stable. If not, it is susceptible to liquefaction. However, retrieval of soil specimens from the field using typical drilling and sampling techniques induces a lot of disturbance, making it difficult to translate laboratory test results onto field conditions. Therefore, semi-empirical relationships have been developed between CRR of sands and the results of in-situ tests (such as penetration tests and shear velocity measurements) by compiling case histories in which evidence of liquefaction had or had not been observed [34, 88].

Figure 1.4 illustrates a schematic of liquefaction charts. The abscissa plots soil properties as determined from in-situ tests, such as relative density, penetration resistance, and shear wave velocity. The ordinate plots the CSR. By plotting case histories on such a chart, it has been observed that cases of liquefaction and non-liquefaction could be roughly demarcated by a boundary. The boundary represents the in-situ CRR of sands.

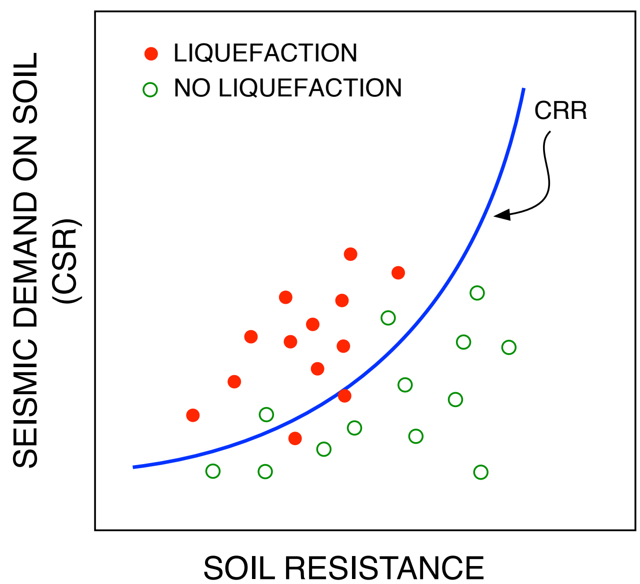

Figure 1.4: Schematic illustrating liquefaction charts. Liquefaction (solid red) and non-liquefaction (open green) case histories are plotted on a graph. Soil resistance can be in terms of relative density, penetration resistance, or shear wave velocity. The two types of case histories can be roughly demarcated by a boundary, which denotes the in-situ CRR of sands.

1.3 Research Objectives

We are now in a position to outline our research objectives. It can be appreciated that liquefaction poses a significant risk to distributed infrastructure systems that are vital for the security, economy, safety, health, and welfare of societies. In order to make our cities more resilient to the effects of liquefaction, it is important to be able to identify areas that are most susceptible. As discussed, conventional slope stability analysis and the use of liquefaction charts help in that endeavor. However, these methodologies have some limitations, which motivate the research objectives for this dissertation.

For instance, liquefaction charts are compiled using case histories, which make them inherently empirical. This limits their scope of application. To reliably extend their scope, high-quality field data are needed. However, field data can only be obtained following earthquake-induced liquefaction. Therefore, it is important to incorporate physics in these charts, so that they can make reliable predictions in the absence of sufficient field data. The first step in that endeavor is to develop a deeper understanding of the fundamental physics of soil liquefaction.

Furthermore, liquefaction charts can only determine the liquefaction susceptibility of a site. They do not inform us about the effects of liquefaction. If a site will liquefy, will it experience flow liquefaction or cyclic mobility? In other words, will liquefaction cause only a slight settlement of foundations or will it cause entire buildings to topple? Liquefaction charts do not make these distinctions. Such information is crucial when it comes to evaluating surface hazards of liquefaction, necessitating a more physical understanding of these charts.

Conventional slope stability analysis assumes that soil will fail under drained conditions, via strain-localization. However, locally undrained conditions can make the slope susceptible to static liquefaction [32, 48]. This contrast in soil behavior due to different drainage conditions poses some questions. For instance, although a dense sand is stable under undrained loading, what happens under partial drainage conditions? How do we estimate the soil strength in that case? Such questions necessitate further research into the subject of static liquefaction.

The most fundamental way to measure soil strength is via laboratory testing. However, retrieval of soil specimens from the field using typical drilling and sampling techniques induces a lot of disturbance, which alters the mechanical properties of soil. As a result, in-situ testing techniques have gained prominence. The discrepancy in mechanical behavior is often attributed to the difference in soil fabric, or grain arrangement, of laboratory soil sample and in-situ soil [34, 70]. In principle, if we can quantify the soil fabric in the laboratory and in-situ, it may be possible to translate laboratory test results to field conditions. However, fabric quantification measures [45] need grain-scale information, making them impractical for quantification of in-situ fabric. This raises a fundamental question – is it possible to quantify in-situ soil fabric at all? If so, how? These are important questions, seeking answers to which require further research.

1.4 Scope of Thesis

The thesis is organized as follows. Chapter 2 focuses on developing a deeper understanding of the fundamental physics of soil liquefaction. This is achieved by investigating what is perhaps the simplest manifestation of liquefaction, namely static loading in a triaxial compression test. Specifically, the chapter addresses the mechanics of origin of flow liquefaction instability in a triaxial compression test, under static, or monotonic loading. It defines a flow liquefaction potential that helps understand why certain soils liquefy under certain conditions. It also proposes a necessary precursor, or warning sign, prior to the onset of flow liquefaction. The validity of the flow liquefaction potential and necessary precursor were checked using discrete element method simulations [17].

Chapter 3 numerically investigates the mechanics of liquefaction charts, and proposes flow liquefaction as a mechanism for the lower end of these charts. This yields a more physical understanding of such charts and can provide an engineer additional information regarding the effects of liquefaction. The numerical tool employed was the Dafalias-Manzari model [18], which is a continuum plasticity model.

Chapter 4 investigates the effect of fabric on shear wave velocity V_S in soils. As mentioned in section 1.2, V_S is one of the indices that are used for quantifying soil resistance to liquefaction. In essence, it acts as a proxy for parameters affecting soil behavior, such as relative density and confining stress. By understanding how fabric affects V_S, V_S may also be able to act as a proxy for soil fabric, and help in quantification of in-situ soil fabric. Quantification of in-situ soil fabric may enable investigators to translate laboratory test results on to field conditions, with greater certainty. This investigation was numerically performed using the level sets discrete element method [39, 41].

Finally, Chapter 5 summarizes some key developments of this dissertation.

Chapters 2, 3, and 4 can be read independently. Chapter 2 is a published article [58], while Chapters 3 and 4 have been submitted [59, 60] to journals for possible publication. Due to the independent nature of these chapters, there is invariably some content repetition.

Chapter 2

MECHANICS OF ORIGIN OF FLOW LIQUEFACTION INSTABILITY UNDER PROPORTIONAL STRAIN TRIAXIAL COMPRESSION

[1] U. Mital and J.E. Andrade. "Mechanics of origin of flow liquefaction instability under proportional strain triaxial compression". In: *Acta Geotechnica* (2016), pp. 1–11. DOI: 10.1007/s11440-015-0430-8. URL: http://link.springer.com/article/10.1007/s11440-015-0430-8/fulltext.html.

2.1 Introduction

Liquefaction is a field-scale phenomenon, typically associated with earthquake-induced shaking, that causes a loss of strength of saturated cohesionless granular media. It can lead to catastrophes such as landslides, tilting and settlement of buildings, and failure of dams, bridges, and retaining walls [27]. Typically, liquefaction can be divided into flow liquefaction and cyclic mobility [27, 44]. The US National Academy of Science's National Research Council [27] defined flow liquefaction as, "the condition where a a soil mass can deform continuously under a shear stress less than or equal to the static shear stress applied to it." Flow liquefaction is the more devastating manifestation of liquefaction that can lead to field-scale catastrophes. Cyclic mobility, on the other hand, is a more benign form of liquefaction which does not lead to loss of stability.

Although primarily associated with earthquakes, flow liquefaction has been shown to occur under both static and dynamic loading [36, 44, 48, 79]. It occurs when the shear stress required for static equilibrium of a soil mass is greater than the shear strength of the soil in its liquefied state [44]. Given its consequences, it is important to not only understand this phenomenon, but also what causes it in the first place. Although progress has been made in understanding the macro and micro mechanics at the onset of flow liquefaction instability [3, 19, 20, 22, 42, 66], our understanding of the *origin* of this phenomenon is still incomplete. For instance, why are loose sands susceptible to flow liquefaction under undrained conditions [44]? How much increase in pore pressure is sufficient to induce liquefaction, and why does the amount vary under different initial conditions [44]?. In addition, it is usual to assume that flow liquefaction instability occurs under completely undrained or constant volume conditions. However, there is evidence [27, 53, 69, 84] to suggest that soil may undergo volume changes during earthquake shaking. Under static loading, a soil may be experiencing volume changes due to unequal pore pressure generation in adjacent soil layers of different densities [80, 84]. Flow liquefaction under such conditions cannot be attributed to constant volume deformations. Our central objective is to address the aforementioned issues by investigating the origins of flow liquefaction instability under proportional strain triaxial compression conditions.

We start by defining a flow liquefaction potential for determining flow liquefaction susceptibility during proportional strain triaxial compression. A proportional strain triaxial test is one in which the imposed volume change (or the imposed dilatancy) is proportional to the axial strain on the soil specimen. If the volume is imposed to be constant (isochoric strain compression), then the test becomes an undrained triaxial test [21]. The flow liquefaction potential is a function of inconsistency between the natural dilative tendency of the soil and the imposed dilatancy during proportional strain triaxial compression. Such a potential has been used previously [21]. Previous works also imply that [19–22, 42] that given the right conditions, a loose soil that contracts during drained triaxial compression and liquefies under undrained triaxial compression may be stable under proportional strain triaxial compression. Conversely, a dense soil that dilates during drained triaxial compression and is stable under undrained triaxial compression may liquefy under proportional strain triaxial compression. The undrained loose case is a special case of proportional strain triaxial compression under which a soil can liquefy. By analyzing the defined flow liquefaction potential, we provide an interpretation about the micromechanics at play which make a soil susceptible to flow liquefaction. Furthermore, we also analyze stress evolution during proportional strain triaxial compression and discuss the mechanics of the test leading up to flow liquefaction instability. We arrive at a necessary precursor for instability, which can serve as a warning sign for flow liquefaction instability under proportional strain triaxial compression, whilst the soil is still stable. It is important to note that the precursor is not a condition of sufficiency and should also not be confused with the onset of instability itself. The same loading must be applied continuously to induce flow liquefaction instability. This provides further insight into the mechanics of origin of flow liquefaction instability under proportional strain triaxial compression.

2.2 Soil response under proportional strain triaxial compression

In a proportional strain triaxial compression test, the volumetric strain increment is proportional to the axial strain increment. The undrained triaxial compression test is a special case where the proportion is equal to zero, resulting in a constant volume test. The behavior of soil under proportional strain triaxial compression can be either 'stable' or 'unstable'. Figure 2.1 presents a typical response of soil under proportional strain triaxial compression conditions.

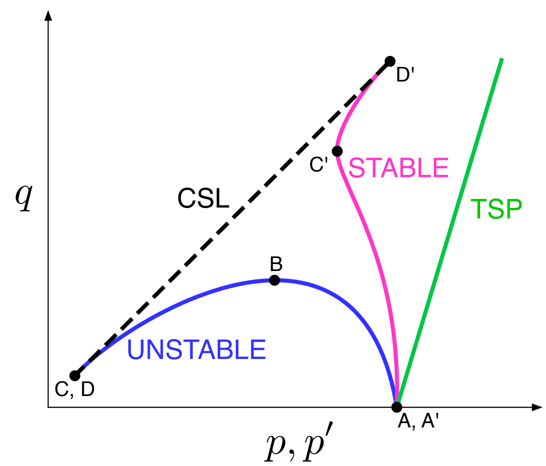

Figure 2.1: Effective stress paths of stable and unstable sands under proportional strain triaxial compression. The total stress path (TSP) and critical state line (CSL) are also sketched for reference. A = start, B = Instability, C = phase transformation, D = critical state. In unstable sands, points C and D are often indistinguishable [36]. A′, C′, and D′ are the corresponding points in a stable sand.

Instability or *unstable* behavior is characterized by loss of deviatoric strength when a soil is subjected to deviatoric strain increments. In case of an undrained triaxial test on a loose sand, this loss of deviatoric strength coincides with the vanishing of second order work, which has been shown to be associated with bursts in kinetic energy and extensive strain softening [19, 22]. This is accompanied by a large pore pressure build up. Under proportional strain triaxial conditions, however, loss of deviatoric strength and vanishing of second order work do not necessarily coincide. To that effect, some investigators have proposed an alternate response parameter whose peak coincides with the vanishing of second order work [19, 20, 22, 42]. In any case, experimental and numerical results of the aforementioned investigators also suggest that along with the vanishing of second order work, loss of deviatoric strength is also a necessary condition for flow liquefaction under proportional strain triaxial conditions in a triaxial test. We will briefly discuss the alternate response parameter in section 2.4. Presently, for the sake of simplicity, we consider the deviatoric stress as a response parameter in our work. Once the soil specimen reaches the peak in effective stress space (characterized by peaking of deviatoric stress), it advances to flow liquefaction failure, assuming that the same loading path is applied continuously. Therefore, a necessary condition for unstable flow liquefaction behavior can be expressed as:

$$\dot{q} < 0 \tag{2.1}$$

where $\dot{q}$ is the deviatoric invariant of the stress rate tensor.

In case of *stable* behavior, the soil specimen may initially exhibit behavior reminiscent of a loose sand under undrained triaxial compression. However, before the soil specimen reaches the peak in effective stress space, it undergoes a phenomenon called 'phase transformation' [36], whereby it starts exhibiting behavior reminiscent of a dilative sand under undrained triaxial compression. This phenomenon ostensibly provides stability, whereby the pore water pressure build-up and strain softening are kept in check.

In what follows, $\dot{\sigma}$ is the stress increment tensor and $\dot{\epsilon}$ is the strain increment tensor. We use subscripts a and r to denote the axial and radial components respectively. $\dot{p} = (\dot{\sigma}_a + 2\dot{\sigma}_r)/3$ and $\dot{q} = (\dot{\sigma}_a - \dot{\sigma}_r)$ are the volumetric and deviatoric invariants of stress increment ($\dot{\sigma}$), respectively. $\dot{\epsilon}_v = (\dot{\epsilon}_a + 2\dot{\epsilon}_r)$, and $\dot{\epsilon}_s = 2(\dot{\epsilon}_a - \dot{\epsilon}_r)/3$ are the volumetric and deviatoric invariants of strain increment ($\dot{\epsilon}$), respectively.

2.3 Flow Liquefaction Potential

In order to determine whether the behavior of a soil specimen under proportional strain triaxial compression will be stable or unstable, we define a *flow liquefaction potential* $\mathcal{L}$. For a soil to be susceptible to unstable flow liquefaction behavior, we postulate that:

$$\mathcal{L} > 0 \tag{2.2}$$

Conversely, for stable soil behavior, we postulate that $\mathcal{L} < 0$. The condition when $\mathcal{L} = 0$ will be discussed later. We define the functional form of $\mathcal{L}$ as:

$$\mathcal{L} = \beta - \beta_p \tag{2.3}$$

where β is the *natural dilative tendency* of the soil specimen, and β_p is the *imposed dilatancy* on the specimen during proportional strain triaxial compression. *Natural* *dilative tendency* may be defined as the volume change that a soil specimen must undergo such that pore pressure does not evolve. The natural dilative tendency of a soil specimen can be determined from its behavior under fully drained conditions. A soil that contracts during drained triaxial compression has $\beta > 0$, while a soil that dilates during drained triaxial compression has $\beta < 0$. On the other hand, *imposed dilatancy* is the volume change *imposed* on a soil specimen during a proportional strain triaxial test, which is normally different from the natural dilative tendency and leads to an evolution in pore pressure. Equation 2.3 is similar to a liquefaction potential defined by Darve and Pal [21]. While Darve and Pal [21] derived the potential using ideas from continuum plasticity, it will become apparent that our potential has been derived by considering imposed radial strain increments.

Mathematically, natural dilative tendency β can be defined as [85]:

$$\beta = \frac{\dot{\epsilon}_v}{\dot{\epsilon}_s} \tag{2.4}$$

where we have assumed elastic strain increments to be negligible. We define imposed dilatancy β_p as:

$$\beta_p = \frac{\dot{\epsilon}_v^p}{\dot{\epsilon}_s^p} \tag{2.5}$$

where the superscript p denotes imposed proportional strain triaxial compression. Note that for imposed dilatancy, we are concerned with total strain increments.

We now take a closer look at drained and proportional strain triaxial compression in order to understand why $\mathcal{L} > 0$ makes a soil susceptible to flow liquefaction instability.

Drained Triaxial Compression

Drainage of pore water ensures that pore pressures do not evolve. It also implies that the granular assembly undergoes changes in volume. Using the definition of β, volumetric strain increment $\dot{\epsilon}_v$ can be expressed as a function of shear strain increment $\dot{\epsilon}_s$:

$$\dot{\epsilon}_v = \beta\dot{\epsilon}_s \tag{2.6}$$

Using the definitions of $\dot{\epsilon}_v$ and $\dot{\epsilon}_s$ from section 2.2, we can obtain the radial strain increment $\dot{\epsilon}_r$ consistent with the natural dilative tendency of the assembly, given an applied axial strain increment $\dot{\epsilon}_a$:

$$\dot{\epsilon}_r = \alpha \dot{\epsilon}_a =: \dot{\epsilon}_r^d \tag{2.7}$$

where α is function of natural dilative tendency β:

$$\alpha = \frac{2\beta - 3}{2\beta + 6} \tag{2.8}$$

Note that $\alpha < 0$. This is because soil has a positive poisson's ratio, implying that compressing the granular assembly in the axial direction will make it expand or stretch out in the radial direction. We have assumed the usual geomechanics convention of compression being positive.

Proportional Strain Triaxial Compression

However, in a proportional strain triaxial compression test, the volumetric strain increment $\dot{\epsilon}_v$ is constrained to be proportional to the axial strain increment $\dot{\epsilon}_a$. Equivalently, we may say that given an applied axial strain increment $\dot{\epsilon}_a$, the radial strain increment $\dot{\epsilon}_r$ is:

$$\dot{\epsilon}_r = \alpha_p \dot{\epsilon}_a =: \dot{\epsilon}_r^p \tag{2.9}$$

where α_p may or may not be constant. For simplicity, it is often imposed as a constant. It may be noted that α_p is similar to R defined in literature [19–22, 42]. Several investigators have devised experimental programs whereby for axisymmetric conditions prevalent in a triaxial test, such strain paths can be imposed [15, 19, 80]. For a saturated sample, volume changes imposed during such strain paths can be associated with injection or extraction of water in the soil sample [20], such that the drainage is incompatible with that during a drained test, leading to pore pressure variation. Such a test has also been referred to as a partially drained test in the past [80].

In any case, the relation between α_p and β_p is same as the relation between α and β (equation 2.8). Therefore, by inverting equation 2.8, the imposed dilatancy β_p can be obtained as a function of α_p:

$$\beta_p = \frac{3(1 + 2\alpha_p)}{2(1 - \alpha_p)} \tag{2.10}$$

The undrained test is a special case where $\alpha_p = -1/2$, yielding $\beta_p = 0$.

We are now in a position to understand how the flow liquefaction potential $\mathcal{L}$ can help in evaluating flow liquefaction susceptibility of a soil subjected to proportional strain triaxial compression. Using equation 2.10, $\mathcal{L}$ can be expressed as a function of α and α_p:

$$\mathcal{L} = \frac{9(\alpha - \alpha_p)}{2(1-\alpha)(1-\alpha_p)} \tag{2.11}$$

Note that a positive poisson's ratio implies $\alpha < 0$. In addition, proportional strain triaxial compression tests are conducted such that $\alpha_p < 0$. Therefore, the denominator in equation 2.11 above is a positive quantity. This means that:

$$\mathrm{sign}(\mathcal{L}) = \mathrm{sign}(\alpha - \alpha_p) \tag{2.12}$$

Equivalently, since both α and α_p are negative:

$$\boxed{\mathrm{sign}(\mathcal{L}) = \mathrm{sign}(|\alpha_p| - |\alpha|)} \tag{2.13}$$

For a soil to be susceptible to flow liquefaction during proportional strain triaxial compression, we postulated that $\mathcal{L} > 0$. This implies that given an axial strain increment $\dot{\epsilon}_a$, the radial strain increments for proportional $\dot{\epsilon}_r^p$ and drained $\dot{\epsilon}_r^d$ triaxial compression are related as:

$$|\dot{\epsilon}_r^p| > |\dot{\epsilon}_r^d| \tag{2.14}$$

where we have used equations 2.7 and 2.9. Equation 2.14 implies that the imposed proportional radial strain increment is more expansive than the drained radial strain increment. Micro-mechanically, this may be interpreted as soil grains pushing outwards and spreading more intensely than the natural dilative tendency. This increases the load on pore water, causing pore water pressure to rise during proportional strain triaxial compression, making the assembly susceptible to flow liquefaction.

Conversely, for a soil to exhibit stable behavior during proportional strain triaxial compression, we postulated that $\mathcal{L} < 0$. This implies that given an axial strain increment $\dot{\epsilon}_a$, the radial strain increments for proportional ($\dot{\epsilon}_r^p$) and drained ($\dot{\epsilon}_r^d$) triaxial compression are related as:

$$|\dot{\epsilon}_r^p| < |\dot{\epsilon}_r^d| \tag{2.15}$$

Equation 2.15 implies that the imposed proportional radial strain increment is less expansive than the drained radial strain increment. Micro-mechanically, this may be interpreted as soil grains pushing outwards less intensely than the natural dilative tendency. The grains tend to coalesce together, creating a pulling or suction effect on the pore water, that causes pore water pressure to fall during proportional strain triaxial compression, making the assembly stable. See Figure 2.2 for a cartoon of the discrepancy in radial strain increments for both $\mathcal{L} > 0$ and $\mathcal{L} < 0$.

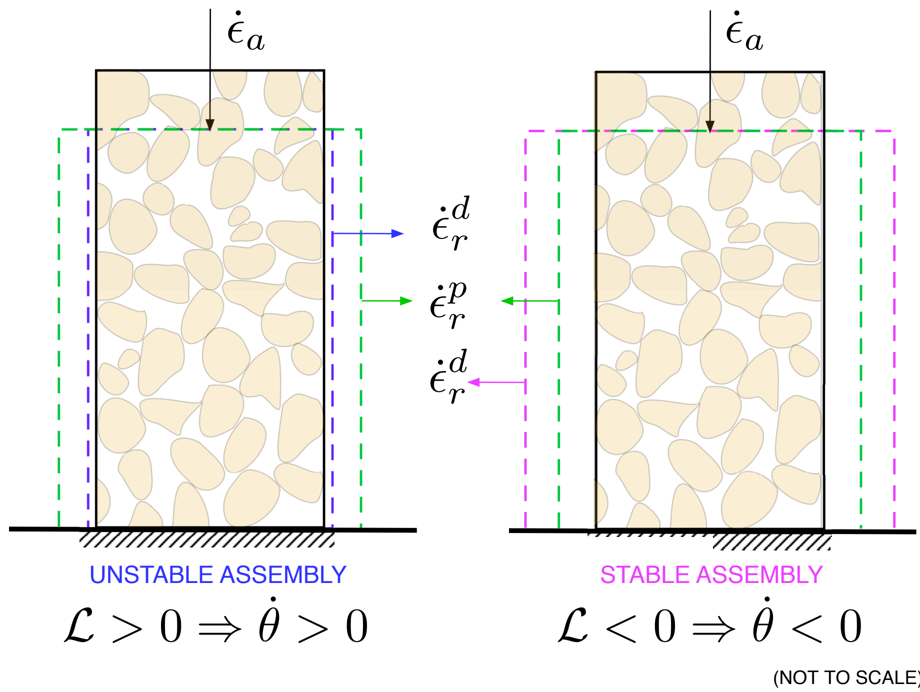

Figure 2.2: Cartoon showing the mismatch between the imposed proportional ($\dot{\epsilon}_r^p$) and the drained ($\dot{\epsilon}_r^d$) radial strain increments, given an axial strain increment ($\dot{\epsilon}_a$). In an unstable assembly, $\mathcal{L} > 0$, which means that the imposed radial strain increments are more expansive than the natural dilative tendency. As a result, soil grains push outward and spread more intensely than the natural dilative tendency. This increases the load on pore water, causing pore water pressure to rise ($\dot{\theta} > 0$). Conversely, for a stable assembly, $\mathcal{L} < 0$, which means that soil grains push outwards less intensely than the natural dilative tendency. The grains tend to coalesce together, creating a pulling or suction effect on the pore water, which causes pore water pressure to fall ($\dot{\theta} < 0$).

Undrained Triaxial Compression

As we mentioned earlier, undrained triaxial compression is a special case of proportional strain triaxial compression where $\beta_p = 0$, implying $\mathcal{L} = \beta$. Therefore, a soil that contracts during drained triaxial compression ($\beta > 0$) is susceptible to flow liquefaction under undrained triaxial compression, whereas a soil that dilates during drained triaxial compression ($\beta < 0$) exhibits stable behavior under undrained triaxial compression.

Discussion

It is important to note that given the right conditions, a loose soil that contracts during drained triaxial compression and liquefies under undrained triaxial compression may be stable under proportional strain triaxial compression. Conversely, a dense soil that dilates during drained triaxial compression and is stable under undrained triaxial compression, may liquefy under proportional strain triaxial compression. Such loading conditions can occur in the field when there are soil layers of different densities adjacent to each other. Susceptibility to flow liquefaction instability is determined not by the sign of β, but by the sign of $\mathcal{L}$. Depending on the imposed β_p, the sign of $\mathcal{L}$ can change. Figure 2.3 shows how negative (or expansive) values of β_p increase $\mathcal{L}$, while positive (or contractive) values of β_p reduce $\mathcal{L}$. It just so happens that during undrained triaxial compression, since $\beta_p = 0$, the sign of β determines the sign of $\mathcal{L}$. Stable response of loose sands and unstable response of dense sands under proportional strain triaxial compression have been observed in experimental and numerical studies in the past [15, 19–22, 42, 80]. Note that $\mathcal{L} > 0$ signifies a potential to liquefy. It does not sufficiently imply occurrence of flow liquefaction. Sustained loading with $\mathcal{L} > 0$ is necessary for the soil to encounter flow liquefaction instability. Finally, note that $\mathcal{L} = 0$ implies that the imposed dilatancy β_p on the soil specimen is equal to the natural dilative tendency β of the assembly. If such a situation arises, the specimen will behave as if under drained triaxial compression, and pore pressure will not change.

2.4 Necessary precursor for onset of flow liquefaction instability

As mentioned in the introduction, the central objective of this paper is to investigate the origins of flow liquefaction instability. We do so by analyzing the phenomenon under proportional strain triaxial compression. We discussed that if $\mathcal{L} > 0$, then the imposed radial strain increment is more expansive than the drained radial strain increment, which has the effect of increasing the pore pressure. However, it is well known that rise in pore pressure is necessary but not sufficient to cause flow liquefaction instability. For instance, in the case of a dense sand subjected to undrained triaxial compression, pore pressure initially rises, but following phase transformation, $\mathcal{L} < 0$ and pore pressure falls. To address this issue, we now analyze the stress evolution during proportional strain triaxial compression and arrive at a nec-

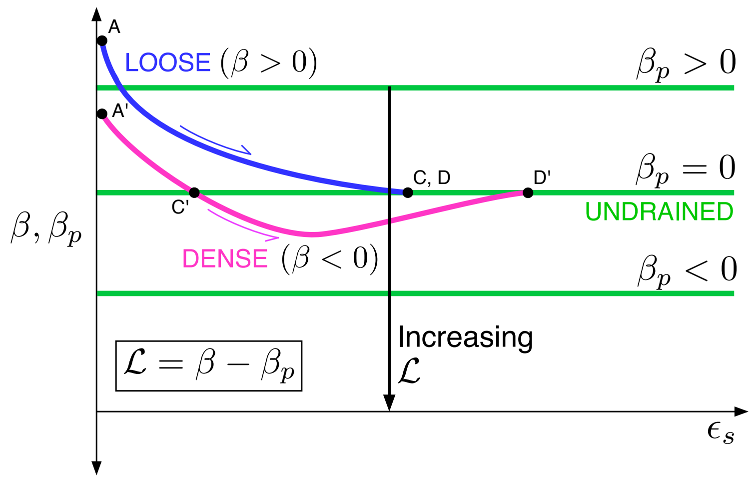

Figure 2.3: Dilative tendencies of loose and dense sand during drained triaxial compression. A = start, C = Phase Transformation, D = Critical state. The primes indicate similar stages for dense sand. $\beta > 0$ indicates contraction during drained triaxial compression, $\beta < 0$ indicates dilation during drained triaxial compression. Proportional strain triaxial compression imposes a volume change that is inconsistent with the natural dilative tendency. If $\beta_p = 0$, a loose soil is susceptible to flow liquefaction while a dense soil exhibits stable behavior. For $\beta_p < 0$, even a dense soil can become susceptible to flow liquefaction. For $\beta_p > 0$, even a loose soil can exhibit stable behavior.

essary precursor for the origin of flow liquefaction instability. This provides further insight into the mechanics of origin of flow liquefaction instability under proportional strain triaxial compression. We first consider the special case of an undrained triaxial compression test, for which the onset of flow liquefaction instability (equation 2.1) can be expressed as a function of *total* axial ($\dot{\sigma}_a$) and radial stress ($\dot{\sigma}_r$) increments, as well as *effective* axial ($\dot{\sigma}'_a$) and radial stress ($\dot{\sigma}'_r$) increments:

$$\dot{q} < 0 \quad \Rightarrow \quad \dot{\sigma}_a - \dot{\sigma}_r < 0 \quad \Rightarrow \quad \dot{\sigma}'_a - \dot{\sigma}'_r < 0 \tag{2.16}$$

Boundary condition imposes constant *total* radial stresses ($\dot{\sigma}_r = 0$). This implies:

$$\dot{\sigma}'_r = \cancel{\dot{\sigma}_r} - \dot{\theta} \quad \Rightarrow \quad \boxed{\dot{\sigma}'_r = -\dot{\theta}} \tag{2.17}$$

where $\dot{\theta}$ is the pore pressure increment. The instability criterion can now be expressed as:

$$\dot{\sigma}'_a + \dot{\theta} < 0 \tag{2.18}$$

Note that $\mathcal{L} > 0$ implies $\dot{\theta} > 0$. Therefore, we need $\dot{\sigma}'_a < 0$ to satisfy the above equation. We now arrive at a *necessary precursor for flow liquefaction instability* during undrained triaxial compression:

$$\boxed{\dot{\sigma}'_a < 0} \tag{2.19}$$

Equation 2.19 suggests that during an undrained triaxial compression test, a soil specimen may encounter flow liquefaction instability only if it is undergoing a reduction in effective axial stress, hereby referred to as axial softening. Prevalence of axial softening prior to onset of instability has been documented in the past [21].

Remark 1: It must be noted that equation 2.19 by itself is necessary but not a sufficient condition for flow liquefaction instability under proportional strain triaxial compression. It is possible for the assembly to be softening axially, yet still be stable. As long as $\dot{q} > 0$, an assembly will be stable despite axial softening. Onset of axial softening can be thought of as a warning sign. If the same loading is applied continuously (sufficiency condition) despite axial softening (necessity condition), then as long as $\mathcal{L} > 0$, pore pressure will continue to rise and onset of instability is inevitable. If loading conditions are changed such that $\mathcal{L} < 0$, pore pressure will drop and the soil will exhibit stable behavior. Also, note that in this context, axial softening should not be confused with the vanishing of hardening modulus as in elasto-plasticity theory.

Remark 2: It must also be noted that not all soils are capable of existing in liquefiable states. Clays, for instance, are inherently non-liquefiable [44]. Axial softening in clays should not be taken as a precursor to flow liquefaction instability. Care must be taken to ensure that the soil in question satisfies the compositional criteria [44] that make it capable of existing in a liquefiable state.

Geometrical argument for necessity of $\dot{\sigma}'_a < 0$

To get a more geometrical perspective of equation 2.19, we refer to Figure 2.4a that shows the evolution of various stress parameters, when a sand is subjected to undrained triaxial compression such that $\mathcal{L} > 0$. Note that for $\dot{q} = 0$, we need $\dot{\sigma}'_a = \dot{\sigma}'_r$. This means that we need the slopes of σ'_a and σ'_r to be equal. From equation 2.17, we know that the slope of σ'_r is always negative. Therefore, the only way the two slopes can be equal is if the slope of σ'_a becomes negative at some point.

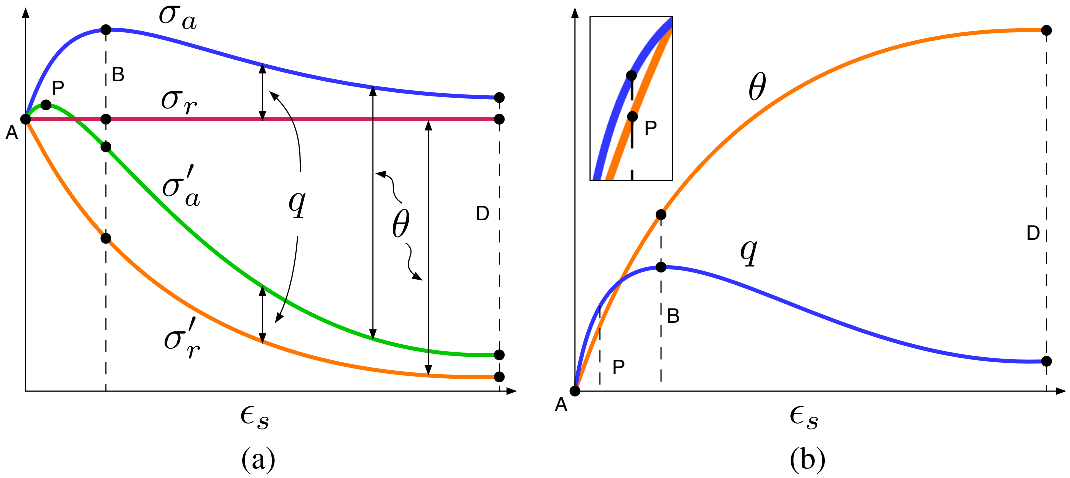

Figure 2.4: Undrained triaxial compression behavior when $\mathcal{L} > 0$. A = start, P = Precursor to instability ($\dot{q} \leq \dot{\theta}$, $\dot{\sigma}'_a \leq 0$), B = Instability, D = Critical State. (a) Evolution of total and effective axial and radial stresses. Before P: $\dot{\sigma}'_a > 0$. After P: $\dot{\sigma}'_a < 0$. (b) Evolution of deviatoric invariant q and pore pressure θ. Before P: $\dot{q} > \dot{\theta}$. After P: $\dot{q} < \dot{\theta}$.

Extension to proportional strain triaxial compression test

As mentioned earlier, some investigators [19, 20, 22, 42] prefer the use of an alternate response variable to mark the onset of instability for a proportional strain triaxial test. The alternate response variable can be expressed as $\xi = \sigma'_a + 2\alpha_p\sigma'_r$ such that $\dot{\xi} = 0$ coincides with the loss of second order work and marks the onset of flow liquefaction instability; here $\alpha_p < 0$ and is defined in section 2.3. Under undrained conditions, ξ reduces to q. Since the total radial stress is constant, $\dot{\sigma}'_r = -\dot{\theta}$ and it can be easily shown that even for $\dot{\xi} < 0$ to be true, $\dot{\sigma}'_a < 0$ is a necessary precursor. Therefore, $\dot{\sigma}'_a < 0$ is a necessary precursor for onset of flow liquefaction stability in a proportional strain triaxial compression test.

Excess pore pressures

Since $\dot{\sigma}_r = 0$, we get $\dot{q} = \dot{\sigma}_a$. We can thus express $\dot{\sigma}'_a$ as:

$$\dot{\sigma}'_a = \dot{q} - \dot{\theta} \tag{2.20}$$

Axial softening ($\dot{\sigma}'_a < 0$) implies:

$$\boxed{\dot{q} < \dot{\theta}} \tag{2.21}$$

Equation 2.21 presents an alternative form of the necessary precursor for flow liquefaction instability under proportional strain triaxial compression. It suggests that *axial softening or loss of effective axial stress occurs when the pore pressure increment is greater than the increment in deviatoric strength* (Figure 2.4b). Note that as long as $\dot{q} > \dot{\theta}$, pore pressure rise will be in check and there will be no axial softening. This can be also be seen in the experimental results of Castro [13]. Mathematically, equations 2.19 and 2.21 are equivalent. Also, note that while deriving equation 2.21 from equation 2.19, we did not make any assumptions about the imposed strain path. Therefore, equation 2.21 holds for any proportional strain path in a triaxial test, not just the isochoric (or undrained) strain path.

Discussion

We belabor the importance of equation 2.19 (or 2.21) with some historical perspective. We refer to Figure 2.4. In the past, liquefaction was analyzed at point D. Thereafter, the concept of flow liquefaction instability was defined whereby point B was thought to be crucial to understanding liquefaction. The instability concept has proven to be very useful and a lot of progress has been made in understanding the macro and micro mechanics at the onset of flow liquefaction instability [3, 19, 20, 22, 42, 66]. Now, we propose that significance should also be given to point P since attainment of point P is a necessary precursor for getting to point B, assuming the same loading is applied continuously (sufficiency condition). The concept of a precursor has potential to further improve our understanding of origin of flow liquefaction. For instance, equation 2.21 sheds some light on the stable behavior of soil when $\mathcal{L} < 0$ (such as dilative assemblies under undrained conditions). In such assemblies, pore pressures drop ($\dot{\theta} < 0$). Since the assembly continues to strengthen, $\dot{q} > \dot{\theta}$ is always true and the necessary precursor for onset of instability is not met.

Remark 3: Note that the proposed necessary precursor is only applicable under idealized condition of proportional strain triaxial compression. An understanding of the physics underlying the origin of flow liquefaction instability under idealized conditions provides us with motivation to look for precursors to instability under different loading conditions, such as soil subjected to constant deviator stress loading, or a soil under more complex and general field conditions. Such a concept could prove to be very useful while monitoring static liquefaction in the field such as slope stability and landslides.

Remark 4: Although Figure 2.4 assumes an isotropic initial state of stress, the result should apply to anisotropic initial state of stress as well, since no assumptions were made about the initial stress state. However, in the case of an anisotropic initial stress state, it is possible that the soil may be susceptible to spontaneous liquefaction, whereby there is a rapid drop in deviator stress at the onset of undrained or proportional strain loading (e.g. [80]). In such a case it may not be possible to detect the aforementioned precursors. Although equations 2.19 and 2.21 will still be satisfied, they may not be able to serve as precursors or warning signs.

2.5 DEM Simulations

The objective of this section is to present simulation results to support our analysis. To that effect, we performed discrete element method (DEM) simulations. DEM is a numerical model that describes the mechanics of an assembly of particles [17]. We'll first briefly describe the contact model and then describe our simulations.

Description of the contact model

Figure 2.5 shows the schematics of the model employed to describe the contact between two particles. The microscopic constants used in the simulations are summarized in table 2.1.

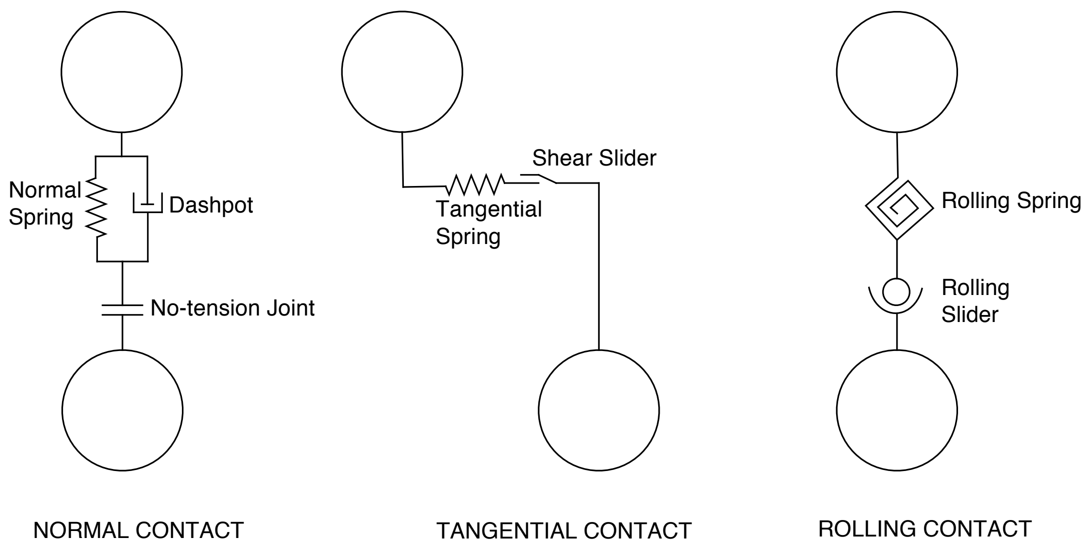

Figure 2.5: DEM contact model

The simulations were modeled after [29]. We employed the MechSys programming library to implement our DEM simulations.

Simulations

We simulated a polydisperse assembly of 1290 particles. The radii of the particles were uniformly distributed within a range of 0.05 to 0.5 cm. We simulated loose

Table 2.1: Microscopic constants used in the simulations.

Constant	Description
K_n = 5000 kN/m	Contact normal stiffness
K_t = 2500 kN/m	Contact tangential stiffness
$\mu = 0.3$	Microscopic friction coefficient
$G_n = 0.16\ s^{-1}$	Normal viscous coefficient
$G_t = 0.0\ s^{-1}$	Tangential viscous coefficient
$\xi = 0.12$	Rolling resistance stiffness
$\eta = 1.0$	Plastic moment coefficient

assemblies and dense assemblies. All assemblies were prepared by subjecting a virgin assembly to isotropic consolidation under drained conditions. Loose assemblies were obtained by isotropically consolidating an assembly to 100 kPa. Dense assemblies were obtained by isotropically consolidating an assembly to 700 kPa and then unloading it back to 100 kPa (giving us an over-consolidated assembly). All tests were conducted using dry spheres. Drained triaxial compression conditions were approximated by imposing a constant total radial stress (σ_r = 100 kPa), and subjecting the assembly to axial strain increments. Proportional strain triaxial compression conditions were simulated by subjecting the assembly to an imposed dilatancy β_p, wherein the radial strain increment is proportional to the axial strain increment. Equivalent pore pressures were inferred using equation 2.17.

Results

Figure 2.6 shows the stress-path of 'loose' and 'dense' soil under drained and undrained triaxial compression conditions. Undrained triaxial compression is a special case of proportional strain triaxial compression where the imposed dilatancy $\beta_p = 0$. As expected, under undrained triaxial compression, loose sands exhibit unstable behavior, whereas dense sands exhibit stable behavior.

In addition to undrained triaxial compression, we also simulated proportional strain triaxial compression tests with an imposed dilatancy of (i) $\beta_p = 0.6$, and (ii) $\beta_p = -0.43$. We verify that given the right conditions, a loose soil that liquefies under undrained triaxial compression, may be stable under proportional strain triaxial compression. Conversely, a dense soil that is stable under undrained triaxial compression may liquefy under proportional strain triaxial compression. Figure 2.7

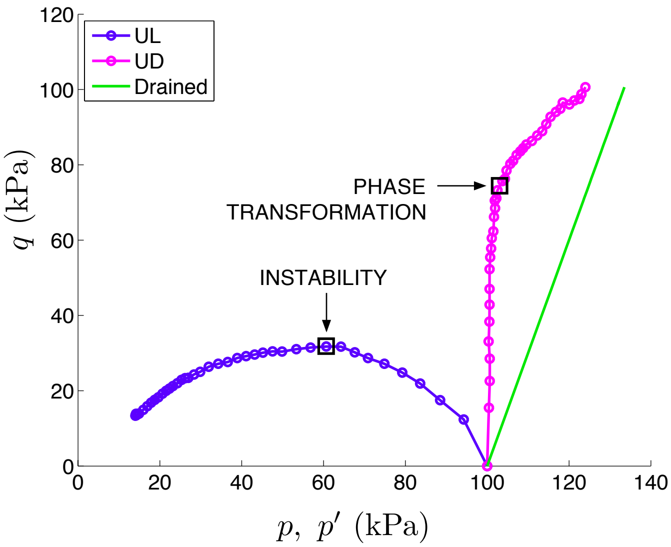

Figure 2.6: Evolution of stresses in the four sets of assemblies. UL: undrained loose, UD: undrained dense. Note the occurrence of instability and phase transformation in the UL and UD assemblies respectively.

shows the volume change or natural dilative tendency β of the 'loose' and 'dense' assemblies under drained triaxial compression. In addition, it also shows the imposed dilatancy β_p during proportional strain triaxial tests. Note that for $\beta_p = 0.6$, the flow liquefaction potential $\mathcal{L}$ reduces for both loose and dense assemblies. Conversely, for $\beta = -0.43$, $\mathcal{L}$ increases for both assemblies. The imposed dilatancy line forms a datum from which one can determine $\mathcal{L}$. If $\mathcal{L} > 0$, pore pressures rise. If $\mathcal{L} < 0$, pore pressures drop. Figure 2.7 also shows that the loose sample has a much higher susceptibility for liquefaction, something well known from experimental observations, but that can be clearly quantified by measuring the dilatancy inconsistency $\beta - \beta_p$, which we call the flow liquefaction potential $\mathcal{L}$. $\mathcal{L}$ helps to visualize how a dense sample can become susceptible to liquefaction, and how a loose sample can exhibit stable behavior.

Figure 2.8 shows the behavior of 'loose' and 'dense' assemblies under proportional strain triaxial compression. As expected from Figure 2.7, $\beta_p = 0.6$ stabilizes the assemblies, while $\beta_p = -0.43$ makes them unstable.

Finally, we demonstrate the plausibility of axial softening (or reduction of effective axial stress) as a necessary precursor for onset of instability. Figure 2.9 shows the evolution of total and effective axial and radial stresses for an unstable assembly.

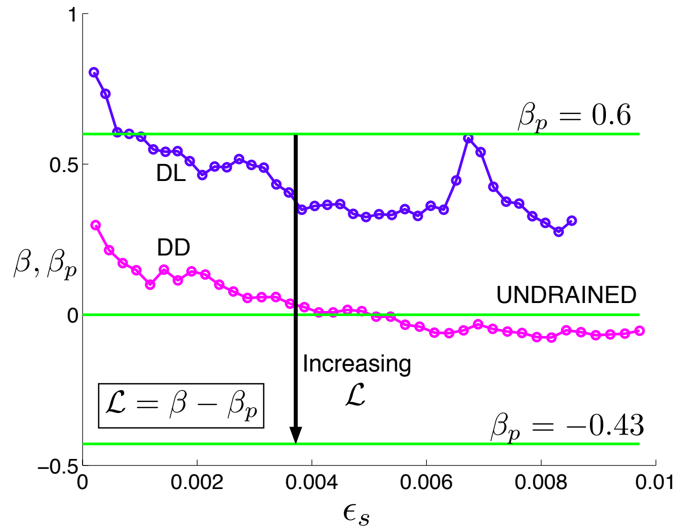

Figure 2.7: Natural dilative tendency (β) in loose and dense assemblies vs imposed dilatancy (β_p). DL: drained loose, DD: drained dense. Note the inconsistency of β_p with β. For $\beta_p = 0.6$, the flow liquefaction potential $\mathcal{L}$ reduces for both loose and dense assemblies. Conversely, for $\beta = -0.43$, $\mathcal{L}$ increases for both assemblies. The imposed dilatancy line forms a datum from which one can determine $\mathcal{L}$. If $\mathcal{L} > 0$, pore pressures rise, making an assembly susceptible to flow liquefaction. If $\mathcal{L} < 0$, pore pressures drop and the assembly exhibits stable behavior. We also see that the loose sample has a higher susceptibility to flow liquefaction.

In this case, it is a loose assembly under undrained conditions. Figure 2.10 shows likewise for a stable assembly, in this case, a dense assembly under undrained conditions. Note the occurrence of axial softening in the unstable assembly (Figure 2.9a) and lack of it in the stable assembly (Figure 2.10a). Applying the same loading continuously (sufficiency condition) caused the assembly in Figure 2.9 to experience flow liquefaction. The stress evolution in Figures 2.9 and 2.10 occur for any stable/unstable assembly under proportional strain triaxial compression. For instance, a dense assembly that is unstable (for example, if $\beta_p = -0.43$) has stress evolution corresponding to Figure 2.9. A loose assembly that is stable (for example, if $\beta_p = 0.6$) has stress evolution corresponding to Figure 2.10. Furthermore, Figures 2.9b and 2.10b show the clear difference that induces liquefaction in unstable sands and not in stable sands. It is clear that the increment of pore pressures becomes greater than the increment of shear strength at point P, which marks the onset of axial softening as a necessary condition for liquefaction. In stable samples, such as that shown in Figure 2.10, pore pressures rise initially, but not at a rate sufficiently high to provoke axial softening. Note that we have presented simulations only for

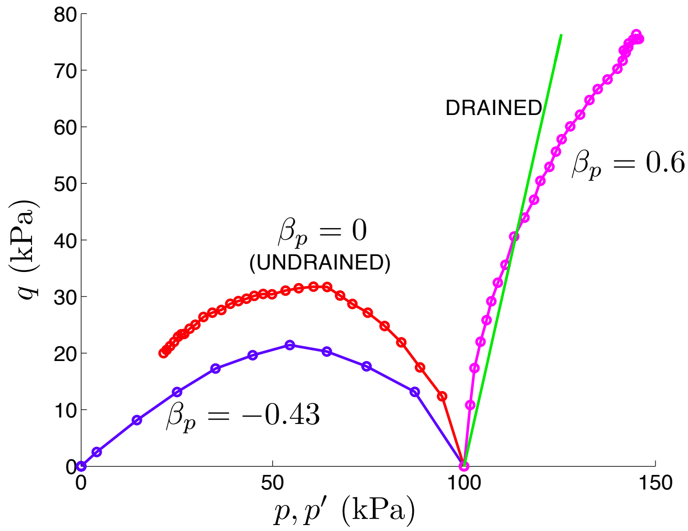

(a)

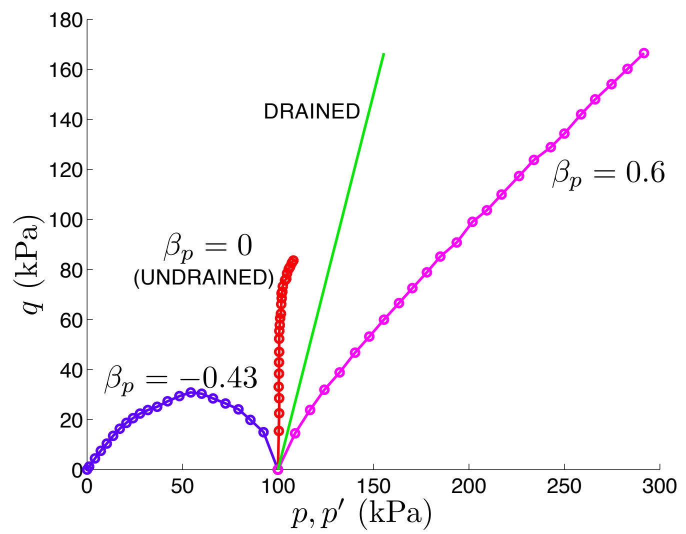

(b)

Figure 2.8: Evolution of stresses under proportional strain triaxial compression. (a) Loose assembly. (b) Dense assembly. Note how $\beta_p = 0.6$ stabilizes the assemblies, while $\beta_p = -0.43$ makes them unstable.

samples with an isotropic initial state of stress. Although our theoretical analysis did not make any assumptions about the initial state, behavior of samples with different initial conditions must still be verified experimentally or numerically.

Remark 5: For the simulation shown in Figure 2.9, axial softening occurs at about 10% of the strain needed for onset of flow liquefaction instability. This shows why

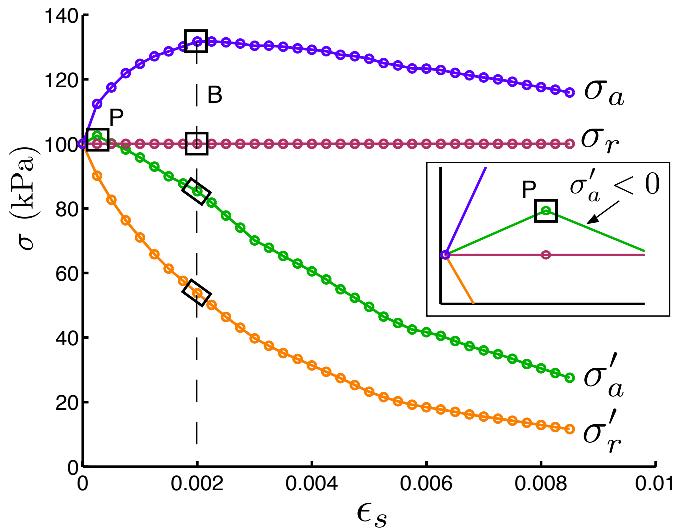

(a)

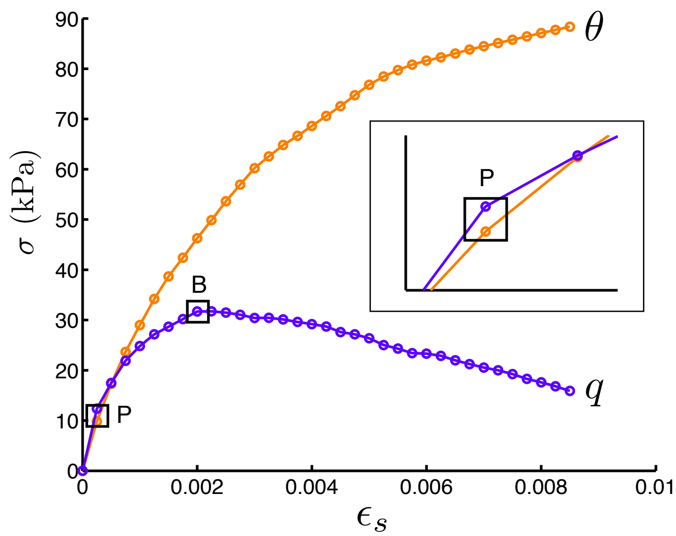

(b)

Figure 2.9: (a) Axial and radial effective and total stresses in an unstable assembly, in this case, loose assembly under undrained triaxial compression. Note the occurrence of axial softening (see inset corresponding to point P) and subsequent instability (B). At instability, note that $\dot{\sigma}'_a = \dot{\sigma}'_r$ and $\dot{\sigma}_a = \dot{\sigma}_r$. (b) Evolution of deviatoric invariant q and pore pressure θ. Before P: $\dot{q} > \dot{\theta}$. After P: $\dot{q} < \dot{\theta}$ (see inset corresponding to point P).

the concept of a necessary precursor is a powerful tool. If the necessary precursor is met, and the same loading is applied continuously (sufficiency condition), then the soil will experience flow liquefaction. This provides us with motivation to investigate and look for necessary precursors under different initial and loading

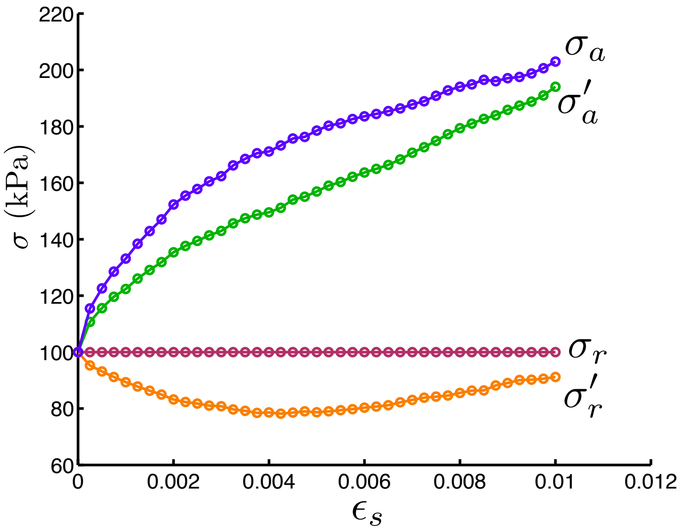

(a)

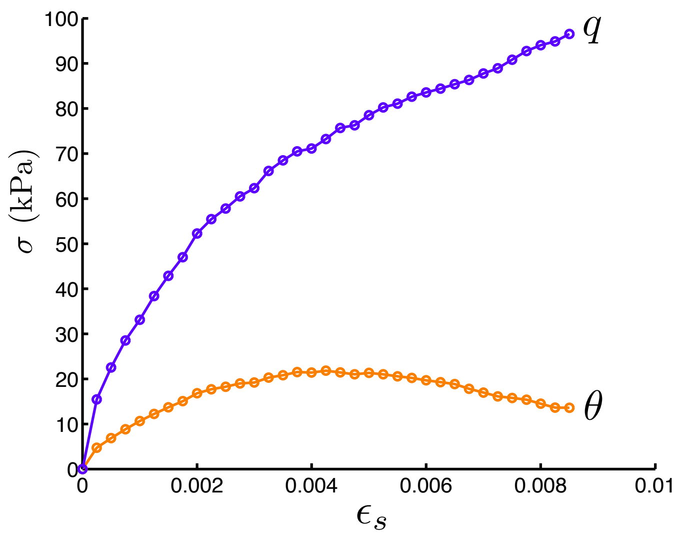

(b)

Figure 2.10: (a) Axial and radial effective and total stresses in a stable assembly, in this case, dense assembly under undrained triaxial compression. Note that there is no axial softening and the assembly continues to strengthen. (b) Evolution of deviatoric invariant q and pore pressure θ. Note that $\dot{q} > \dot{\theta}$ at all times.

conditions. Such a concept could prove to be very useful while monitoring static liquefaction in the field such as slope stability and landslides. If a soil is deemed "at risk" (via some as yet undetermined precursor for field conditions), it could be monitored and steps be taken to mitigate the effects of the instability.

2.6 Conclusions

We defined a new flow liquefaction potential $\mathcal{L}$ for determining flow liquefaction susceptibility during proportional strain triaxial compression. The potential is a function of inconsistency between the natural dilative tendency β and the imposed dilatancy β_p, i.e., $\mathcal{L} = \beta - \beta_p$. If $\mathcal{L} > 0$, pore pressures rise, whereas if $\mathcal{L} < 0$, pore pressures drop. An analysis of $\mathcal{L}$ provided us with a micro-mechanical interpretation of why given the right conditions, a loose soil that contracts during drained triaxial compression and liquefies under undrained triaxial compression, may be stable under proportional strain triaxial compression. Conversely, it also provided us with an interpretation of why a dense soil that dilates during drained triaxial compression and is stable under undrained triaxial compression, may liquefy under proportional strain triaxial compression. The undrained loose case is a special case of proportional strain triaxial compression (where $\beta_p = 0$), under which a soil can liquefy. Flow liquefaction criterion $\mathcal{L}$ provides an elegant framework to visualize how a soil can liquefy despite volume changes; this can happen during seismic shaking in the field, or under static loading when there is differential pore pressure generation between adjacent soil layers with different densities. Unequal pore pressure generation can lead to pore water being injected into certain layers and being extracted from other layers, causing volume changes. Furthermore, since $\mathcal{L} > 0$ is necessary but not sufficient to induce flow liquefaction instability, we analyzed the stress evolution of proportional strain triaxial compression and investigated the mechanics of the test leading up to flow liquefaction instability. We arrived at reduction of effective axial stress (or axial softening) as a necessary precursor for flow liquefaction instability. Axial softening occurs when increment of pore pressure becomes greater than the increment of shear strength. In fact, for the simulation shown in Figure 2.9, axial softening occurs at about 10% of the strain needed for onset of flow liquefaction instability. This shows why the concept of a necessary precursor is a powerful tool. After attaining the precursor, the same loading must be applied continuously (sufficiency condition) for the soil to experience flow liquefaction. This provides us with motivation to investigate and look for necessary precursors under different initial and loading conditions. Such a concept could prove to be very useful while monitoring static liquefaction in the field such as slope stability and landslides. However, if the initial stress state of the soil is such that it is susceptible to spontaneous liquefaction, then the concept of a necessary precursor has limited applicability. Furthermore, care must be taken to ensure that the soil in question satisfies the compositional criteria needed to make it capable of existing in a liquefiable state. For instance, clays are inherently non-liquefiable and will not exhibit liquefaction-like behavior even if they satisfy the necessary precursors. Lastly, note that the term ‘softening’ in this context should not be confused with the vanishing of hardening modulus as in elasto-plasticity theory.

In sum, the current work has taken some important steps towards understanding the mechanics of origin of flow liquefaction instability under proportional strain triaxial conditions. It complements the present understanding of the macro and micro-mechanics at the onset of flow liquefaction instability, and enables a deeper understanding of the phenomenon.

Chapter 3

FLOW LIQUEFACTION INSTABILITY AS A MECHANISM FOR LOWER END OF LIQUEFACTION CHARTS

[1] U. Mital, T. Mohammadnejad, and J.E. Andrade. "Flow liquefaction instability as a mechanism for lower end of liquefaction charts". submitted. 2016.

3.1 Introduction

The state-of-the-practice uses the "simplified procedure" [71] for evaluating liquefaction susceptibility of soils. Based on this procedure, liquefaction charts have been developed that correlate soil resistance to earthquake-induced stresses. Laboratory studies typically quantify soil resistance in terms of void ratio or relative density. On the other hand, field studies typically resort to Standard Penetration Test (SPT), Cone Penetration Test (CPT), or shear wave velocity (V_S) measurements to quantify soil resistance. As pointed out by Dobry and Abdoun [24], this creates a disconnect between laboratory and field measurements. Moreover, liquefaction charts are inherently empirical in nature since they have been developed using case histories. Therefore, there is a poor understanding regarding the underlying physics of these charts, which makes extrapolation into regimes with insufficient case history data difficult. To get the most out of liquefaction charts, it is vital that research be carried out to incorporate more physics in these charts [33]. Studies have been conducted in the past (for example, [9, 10, 24, 33, 78, 79]) to bridge the gap between physics and empiricism. This paper seeks to take another step in that direction.

One of the criticisms of liquefaction charts is that although they give useful information regarding triggering of liquefaction, they do not inform an engineer about the effects of liquefaction [24]. In this paper, we hypothesize that the lower end of liquefaction charts corresponds to unstable flow liquefaction. This informs us about the mechanism of liquefaction at the site, and helps us understand the effects of liquefaction at the lower end of liquefaction charts. In the following sections, we start by reviewing a prevailing explanation about the mechanics of the liquefaction charts [24]. Based on this explanation, we will formulate our hypothesis. Finally, we will present some results of our numerical investigation supporting our hypothesis.

3.2 Background

Recently, Dobry and Abdoun [24] proposed an explanation for the mechanics of the entire liquefaction curve. They proposed that liquefaction charts are essentially a combination of curves of increasing cyclic shear strain (γ_c). If a soil is subjected to N_c cycles of cyclic shear strain greater than γ_c, pore pressure develops leading to liquefaction. The lower end corresponds to normally consolidated sand (K_0 = 0.5) with $\gamma_c \approx$ 0.03-0.05%. The explanation for the upper end is more speculative. It is proposed to correspond to overconsolidated (K_0 = 0.75-1.0), preshaken, and geologically aged sands for which $\gamma_c \approx$ 0.1-0.3%. Note that the requisite cyclic shear strain γ_c for the upper end is approximately 10 times that for the lower end. This is because the pore pressure build-up is much smaller for the upper end. The aforementioned quantities correspond to an earthquake magnitude of M_w = 7 (for which N_c = 10 [71]), and an effective initial confining pressure of p'_0 = 50 kPa. Figure 3.1 presents a summary.

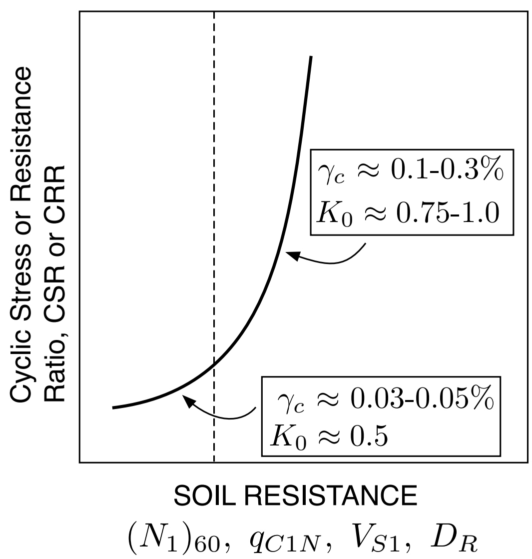

Figure 3.1: Summary of explanation of liquefaction charts as proposed by Dobry and Abdoun [24]. This corresponds to the earthquake magnitude M_w= 7 and the effective initial confining pressure, p'_0 = 50 kPa. Soil resistance can be quantified using either normalized SPT resistance $(N_1)_{60}$, normalized CPT tip resistance q_{C1N}, normalized shear wave velocity V_{S1}, or relative density D_R. The loading experienced by the soil is quantified using the cyclic stress ratio (CSR).

In a triaxial setting, the loading experienced by the soil is quantified using the cyclic stress ratio (CSR), defined as:

$$\text{CSR} = \frac{q_{\text{cyc}}}{2p'_0} \tag{3.1}$$

where q_{cyc} is the the magnitude of uniform cyclic deviatoric stress imposed on the soil sample, and p'_0 is the initial confining pressure. Furthermore, the cyclic stress ratio that is just enough for soil to liquefy is called the cyclic resistance ratio (CRR). The deviatoric stress may be defined as $q = \sigma'_1 - \sigma'_3$, while the confining pressure may be defined as $p' = (\sigma'_1 + 2\sigma'_3)/3$. σ'_1 and σ'_3 are the effective axial and radial stresses, respectively. Note that the initial confining pressure may be either isotropic or anisotropic.

3.3 Mechanics of liquefaction charts

Based on the explanation proposed by Dobry and Abdoun [24], we hypothesize that the lower end of liquefaction charts corresponds to sites that are susceptible to flow liquefaction; while the upper end corresponds to sites susceptible to cyclic mobility. To understand this better, it would be useful to review the definitions of flow liquefaction and cyclic mobility.

Flow liquefaction is an instability that can be triggered at small strains when the applied shear stress is greater than the residual or the steady state strength of the soil [44, 79]. Assuming incompressibility of pore water and undrained loading conditions, the stress path eventually reaches a peak value. Instability is triggered when the soil is loaded beyond the peak of the stress path [44]. This peak also coincides with the vanishing of second order work [31]; under the constraints of undrained loading, that is equivalent to the hardening modulus reaching a limiting value [3, 4], as well as vanishing of the liquefaction matrix [61]. Once instability is triggered, the unstable soil loses strength and undergoes large deformations (Figure 3.2). The confining pressure drops, but may or may not drop all the way to zero.

Cyclic mobility, on the other hand, can occur when the applied shear stress is lower than the residual or the steady state strength of soil [44, 79]. It involves progressive degradation of shear stiffness as the effective pressure drops with each load cycle, leading to accumulation of strains. Unlike flow liquefaction instability, there is no clear-cut point at which cyclic mobility initiates [44]. The strain accumulation seems to accelerate once the effective stress path reaches the steady state line [44, 79]. An empirical criterion to mark the onset of liquefaction (regardless of it being flow liquefaction or cyclic mobility) is the attainment of 3% shear strain [34]. In this work, we will use the 3% strain criterion to mark the onset of cyclic mobility.

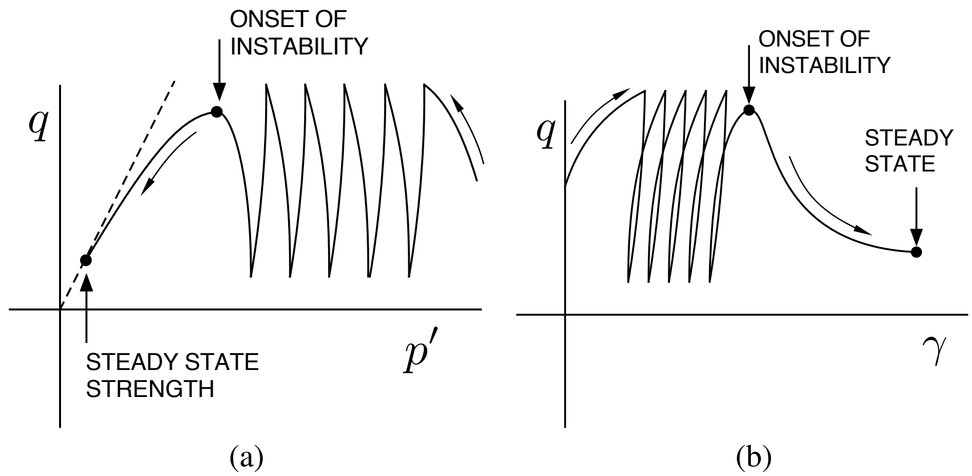

Figure 3.2: Schematic for flow liquefaction during cyclic loading (a): Effective stress path (q vs p'). (b) Shear stress (q) vs shear strain (γ). The dashed line represents the steady state line. Note that the applied shear stress is greater than the steady state strength.

Figure 3.3 shows schematic diagrams of the cyclic mobility phenomenon.

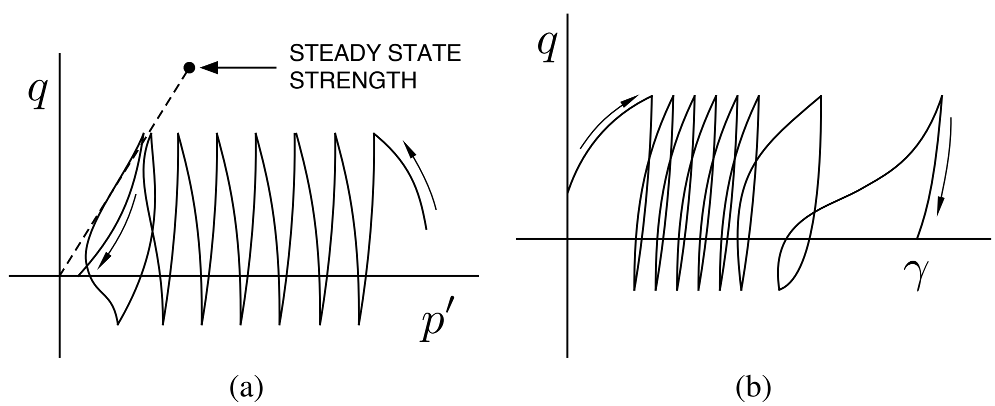

Figure 3.3: Schematic for cyclic mobility during cyclic loading (a): Effective stress path (q vs p'). (b) Shear stress (q) vs shear strain (γ). The dashed line represents the steady state line. Note that the applied shear stress is lower than the steady state strength.

It is important to note that the mechanics of strain accumulation are different for flow liquefaction and cyclic mobility. In the case of flow liquefaction, strains start accumulating rapidly after the onset of instability [44]. After instability, the assembly liquefies of its own accord, following a monotonic path without the need for any external loading. Failure is sudden, signifying a high pore pressure build-up. However, in the case of cyclic mobility, even though strains start accumulating more intensely once the the stress path reaches the steady state line, the strain accumulation is not as intense as during flow liquefaction. The assembly does *not* lose shear strength and become unstable. It needs to be continually subjected to cyclic loading to cause further strain accumulation. If there is stress reversal, the confining pressure may drop to zero. If there is no stress reversal, the stress path simply moves up and down the steady state line [44]. Significant strains may develop over time with a more gradual pore pressure build-up. Note that the shear strain corresponding to steady state in the flow liquefaction case (Figure 3.2) is much larger than the final shear strain shown in the cyclic mobility case (Figure 3.3). However, for the sake of clarity, the difference in their magnitudes has not been highlighted.

Various experimental results show that onset of flow liquefaction instability occurs at values of shear strain lower than 3% (for instance, [14, 37, 76, 81, 86]), which is the empirical strain criterion used to mark the onset of liquefaction[34]. Given that the lower end of liquefaction charts has been proposed to correspond to sites that liquefy at lower values of strain, it seems plausible that the lower end of liquefaction charts corresponds to sites susceptible to unstable flow liquefaction. Similarly, since the upper end of the charts has been proposed to correspond to sites that liquefy at higher values of strains due to a much smaller pore pressure build-up, it seems plausible that the upper end of liquefaction charts corresponds to sites susceptible to cyclic mobility. Figure 3.4 summarizes the proposed hypothesis. In the remaining part of the paper, we numerically investigate the lower end of a relative density based liquefaction chart and also simulate the effect of static shear on a loose soil. These simulations help provide support to our hypothesis.

Liquefaction charts as a function of relative density

Liquefaction charts were first proposed as a function of relative density [72]. Since then, a number of factors other than relative density have been found to be important in evaluating liquefaction resistance. Nevertheless, charts based on relative density still provide valuable insight into liquefaction resistance. It has been pointed out that for recently deposited, normally consolidated, and non-preshaken sands, relative density is strongly correlated to normalized penetration and shear wave velocity values [24]. Since the lower end of liquefaction charts corresponds to normally consolidated sands, relative density can adequately quantify liquefaction resistance of soils corresponding to the lower end of liquefaction charts (for a given soil structure or fabric). In this paper, we use relative density to quantify soil resistance at

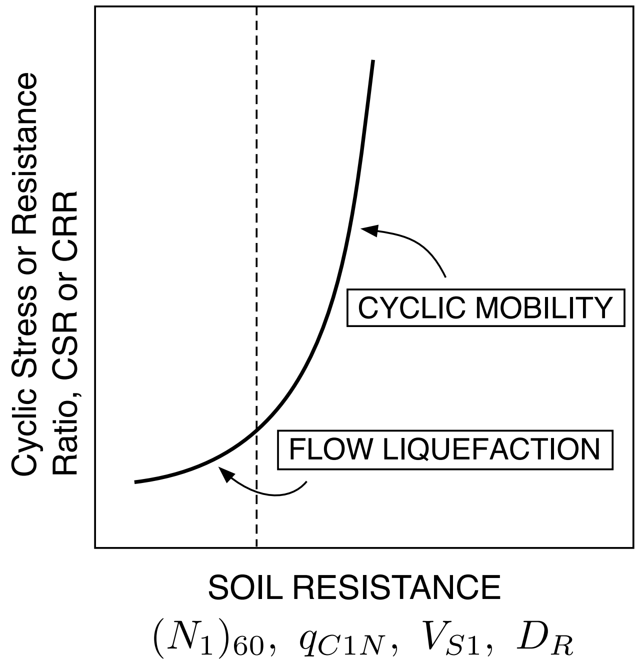

Figure 3.4: Proposed hypothesis. The lower end of liquefaction charts corresponds to flow liquefaction, while the upper end corresponds to cyclic mobility.

the lower end of liquefaction charts.

3.4 Numerical simulations of undrained cyclic triaxial test

We numerically simulated liquefaction in an undrained cyclic triaxial test, using the Dafalias-Manzari plasticity model [18]. The implementation details can be found in [61]. By successively varying the relative density of our numerical soil sample, we obtained a liquefaction chart as a function of relative density. The lower end of the chart was found to correspond to flow liquefaction, which was marked by onset of instability [3, 4, 31, 61]. The upper end did not exhibit unstable behavior and hence the 3% strain criterion was used to flag cyclic mobility [34]. The simulated chart is qualitatively similar to the one obtained by Seed and Peacock [72].

Model calibration

Table 3.1 outlines the parameters used in the Dafalias-Manzari plasticity model [18]. For a brief description of the model parameters, refer to Appendix A. We calibrated the model to some experiments on Ottawa Sand, carried out by Vaid and Chern [79]. Figures 3.5 and 3.6 show some of their results, along with the corresponding simulations which served to calibrate the model. Figure 3.5 corresponds to monotonic loading. The monotonic simulations capture a very important aspect of the experiment, namely the peaking of the stress path in loose sands and phase transformation behavior in the dense sand. Moreover, the location of the steady state line in simulations is very similar to that in experiments. Figure 3.6 corresponds to a cyclic loading experiment. The cyclic simulation captures two important aspects of the experiment. Firstly, flow liquefaction is initiated following the peak in the stress path, which occurs in the 8th cycle. Secondly, the cyclic stress ratio (CSR) (Section 3.2) is the same as that in the experiment. Vaid and Chern [79] expressed their results in a slightly different format and defined CSR as the ratio $(\sigma'_1 - \sigma'_3)/2\sigma'_{3c}$, where σ'_1 and σ'_3 are as defined in Section 3.2 and σ'_{3c} is the initial radial stress. Figure 3.6 uses the definition used by Vaid and Chern [79].

Constant	Variable	Value
Elasticity	G_0	125
	ν	0.05
Critical State	M	1.45
	λ_c	0.065
	e_0	0.722
	ξ	0.9
Yield surface	m	0.01
Plastic modulus	h_0	4.5
	c_h	1.05
	n^b	1.1
Dilatancy	A_0	0.124
	n^d	5.5
Fabric-dilatancy tensor	z_{max}	4
	c_z	600

Table 3.1: Parameters for the Dafalias Manzari Constitutive Model

Simulating the liquefaction chart

In order to simulate the liquefaction chart, each sample had an initial pressure of 100 kPa, and was subjected to 10 loading cycles. Ten loading cycles approximately correspond to an earthquake of magnitude $M_w = 7$ [71]. As discussed in section 3.3, flow liquefaction was deemed to have initiated when the stress path peaked. This also coincides with the vanishing of second order work [31], the hardening modulus reaching a limiting value [3, 4], as well vanishing of the liquefaction matrix [61]. If the stress path did not peak, the cyclic stress ratio (CSR) resulting in 3%

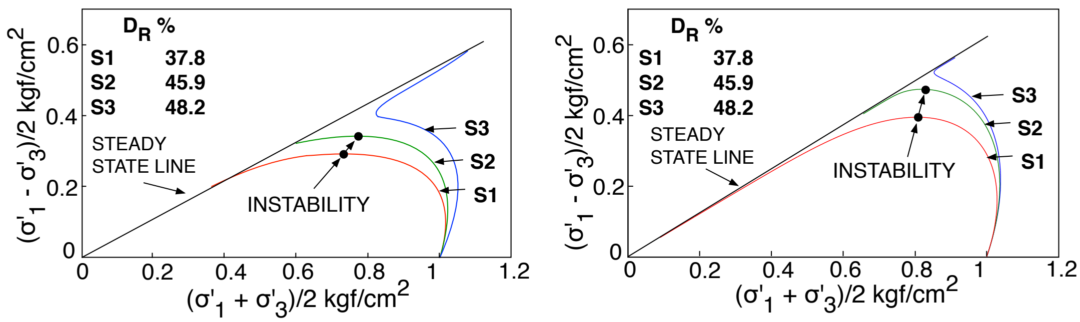

(a) (b)

Figure 3.5: Calibration results for monotonic loading stress paths: (a) Experiments [79]; (b) Simulations

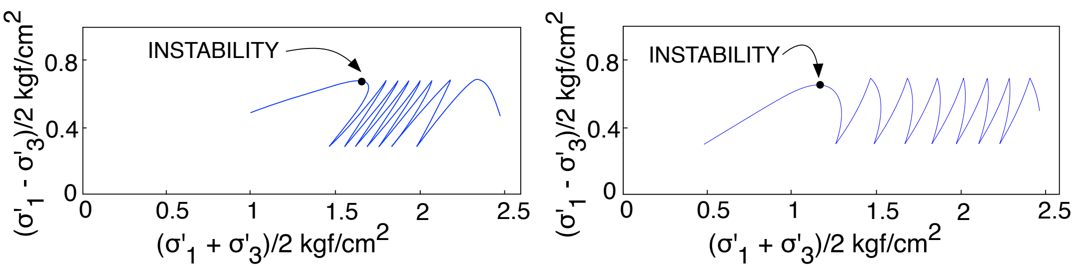

(a) (b)

Figure 3.6: Calibration results for cyclic loading stress path: (a) Experiment [79]; (b) Simulation. The relative density of the soil is 42.8% and CSR is 0.094.

strain [34] was recorded. By successively varying the relative density of the numerical samples, and recording the approporiate CSR, we obtained a liquefaction chart. We picked $K_0 = 0.5$ in order to simulate normally consolidated sand. We picked relative densities over a range of about 30% - 80%. Relative densities lower than a critical value—$D_{R(crit)}$—exhibited unstable flow liquefaction (Figure 3.7). Higher densities made the soil susceptible to cyclic mobility (Figure 3.8). Figure 3.9 shows the liquefaction chart obtained using our simulations, where the lower end ($D_R < D_{R(crit)}$) corresponds to flow liquefaction. In our simulations, $D_{R(crit)}$ was approximately 43%. It may be noted that, qualitatively, this chart is similar to the one proposed by Seed and Peacock [72].

Remark: We would like to point out that although the critical relative density value $D_{R(crit)} \approx 43\%$ forms the boundary between the lower and upper end of the liquefaction chart obtained using our simulations, it should not be taken as a bound-

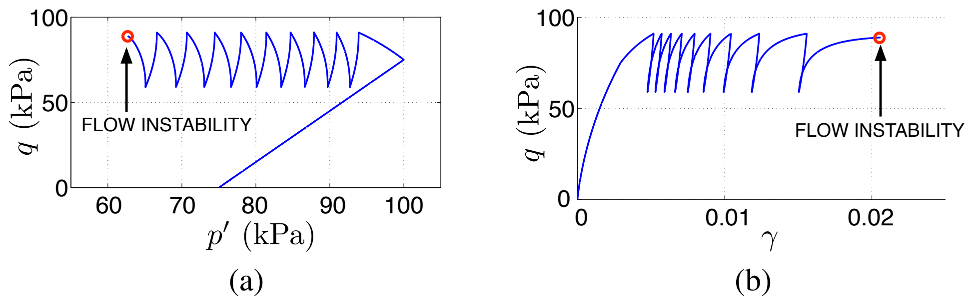

Figure 3.7: (a): Effective stress path for D_R = 42%. (b): Stress-strain path for D_R = 42%. Flow liquefaction instability [4, 31, 61] occurs in the 10th cycle, in this case at a little over 2% strain.

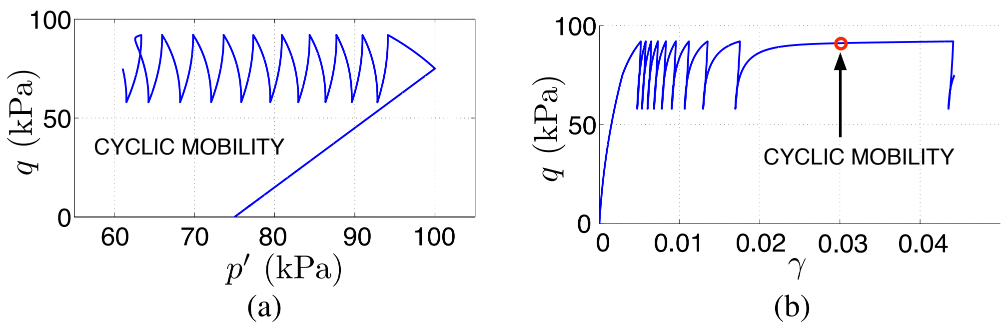

Figure 3.8: (a) Effective stress path for D_R = 44%. (b): Stress-strain path for D_R = 44%. Sample does not become unstable although large strains start accumulating. Onset of cyclic mobility as signified by 3% shear strain occurs in the 10th cycle.

ary between the lower and upper end of liquefaction charts in general. For D_R-based charts, the boundary may vary depending on factors such as the initial stress state, stress history, and fabric of the sand. For the present set of simulations, $D_{R(crit)} \approx$ 43% seems consistent with the experiments to which the model was calibrated[79]. For V_S-based charts, the boundary between lower and upper end may be taken from the study by Dobry and Abdoun [24]. For clean sands, this boundary corresponds to $V_{S1} \approx 160$ m/s. For SPT and CPT-based charts, appropriate correlations developed by Andrus et al. [6] may be used. For clean sands, these may be given by $(N_1)_{60} \approx 15$ and $q_{c1N} \approx 80$.

Simulating effect of static shear stress

Simulating the effect of static shear on a loose soil helps us understand why soils at the lower end of liquefaction charts may be susceptible to unstable flow liquefaction. The effect of static shear is usually quantified by a static shear correction

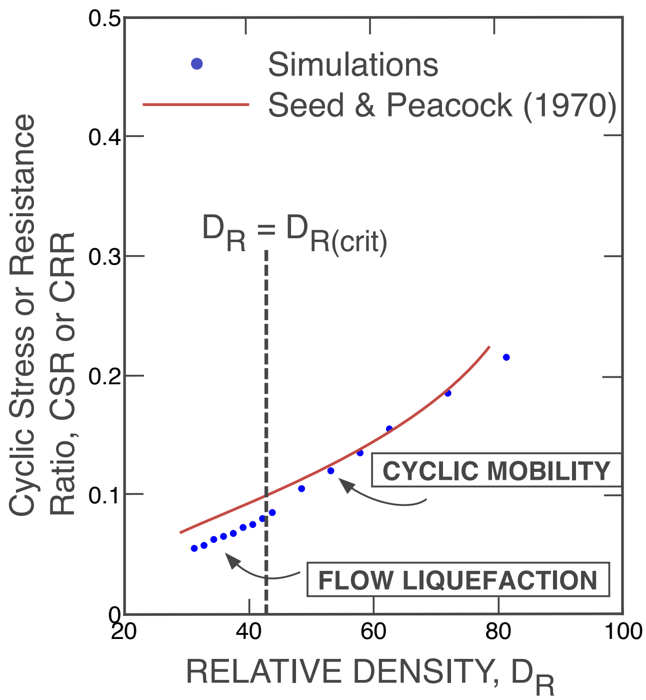

Figure 3.9: Simulated liquefaction chart as a function of relative density; comparison with the Seed and Peacock curve [72]. The critical relative density $\mathrm{D_{R(crit)}}$ separates the chart into a lower and an upper end.

factor K_α, which is defined as:

$$K_\alpha = \frac{\mathrm{CRR}}{\mathrm{CRR}_{\alpha=0}} \tag{3.2}$$

Here, $\alpha = q_s/2p'_0$, where q_s and p'_0 are the values of static shear and effective confining pressure, respectively, at the beginning of cyclic loading. CRR is the cyclic resistance ratio. It is the CSR that is just enough to cause liquefaction. CRR in the numerator is the value associated with the actual value of α, while CRR in the denominator is the value associated with $\alpha = 0$ (isotropic stress state). As will soon become evident, the liquefaction chart simulated in Figure 3.9 corresponds to $\alpha = 0.375$.

We reproduced a K_α curve (Figure 3.10) for $\mathrm{D_R} = 35\%$ under a confining pressure of 100 kPa. This relative density corresponds to the lower end of $\mathrm{D_R}$-based liquefaction chart (Figure 3.9). We obtained a trend similar to the one in the literature for soils with low liquefaction resistance [11, 34, 73].

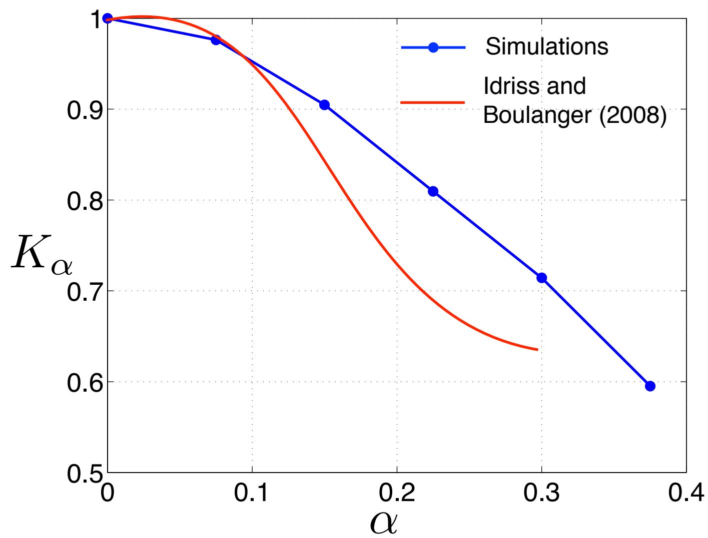

Figure 3.10: Simulated K_α curve for a loose soil (D_R = 35%) corresponding to the lower end of relative density liquefaction chart; comparison with the curve proposed by Boulanger [34]

For the set of simulations in Figure 3.10, α varied from 0 to 0.375. For $\alpha = 0$, the soil exhibited cyclic mobility. For the remaining initial states, the soil was susceptible to flow liquefaction. As pointed out by Vaid and Chern [78, 79], with increasing static shear, loose sands become more susceptible to liquefaction. This can be easily understood using the concept of instability line [78, 79] and collapse envelope [2]. As the quantity of static shear increases, the initial state of the sample moves closer to the instability line, making it more susceptible to flow liquefaction (Figure 3.11).

Figure 3.10 can also be interpreted in terms of the coefficient of earth pressure at rest, or K_0. In a triaxial test, K_0 can be defined as:

$$K_0 = \frac{\sigma'_{30}}{\sigma'_{10}} \tag{3.3}$$

where σ'_{30} is the effective radial stress and σ'_{10} is the effective axial stress prior to undrained loading. It can be shown that in a triaxial test, K_0 and α are related as:

$$K_0 = \frac{3 - 2\alpha}{3 + 4\alpha} \tag{3.4}$$

Physically, $0 < K_0 \leq 1$. Within this range, it can be checked that an increase in α implies a reduction in K_0. This implies that lower values of K_0 make a loose soil more susceptible to flow liquefaction, due to increasing proximity of the initial stress state to the instability line. Specifically, $\alpha = 0.375$ corresponds to $K_0 = 0.5$, which is the coefficient of earth pressure for normally consolidated sand. This implies that a normally consolidated loose soil has an initial stress state that is close to the instability line. Recall that the lower end of liquefaction charts has been proposed to correspond to normally consolidated soils (Section 3.2). Furthermore, as discussed in section 3.3, the lower end of liquefaction charts corresponds to soils with a low relative density, i.e., loose soils. Therefore, Figures 3.10 and 3.11 give further credence to the hypothesis that the lower end of liquefaction charts represent loose soils susceptible to flow liquefaction.

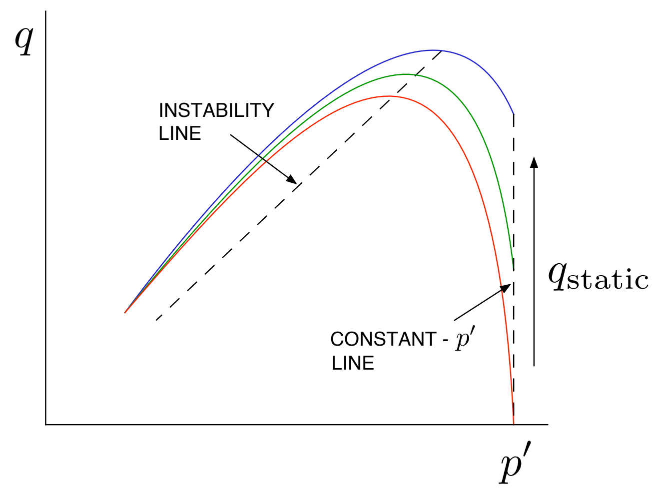

Figure 3.11: Effective stress state diagram for simulating effect of static shear stress. The monotonic stress paths serve as approximate envelopes for cyclic loading stress paths [2]. Note that as the static shear stress (q_{static}) increases, the initial state of the soil moves closer to the instability line.

3.5 Conclusions

The results of our numerical simulations suggest that sites corresponding to the lower end of liquefaction charts are susceptible to flow liquefaction instability. We used relative density to quantify soil resistance. The use of relative density is justified as there is a strong correlation between relative density and penetration values for normally consolidated sands. As proposed by Dobry and Abdoun [24], the lower end of liquefaction charts corresponds to sites that are composed of normally consolidated sands. The work presented in this paper provides additional insight regarding the effects of liquefaction at sites corresponding to the lower end of liquefaction charts. It should be noted that our numerical investigation does not conclusively validate the occurrence of cyclic mobility at the upper end of liquefaction charts, since relative density is not sufficient to estimate liquefaction behavior in that regime. The critical relative density that separates a chart into a lower and an upper end is likely a function of factors like initial stress state, geological and seismic history, and the fabric of sands. A deeper understanding of how such factors affect the critical relative density can provide further insight into the physical mechanism that affects the critical relative density. Regarding sites corresponding to the lower end of liquefaction charts, liquefaction will occur as a consequence of an instability, which will lead to loss of soil strength and large deformations. This is in contrast with cyclic mobility behavior where liquefaction is a consequence of progressive degradation in shear stiffness; soil does not lose stability. As a result, if a site corresponds to the lower end of liquefaction charts, an engineer can estimate not only the loading needed to trigger liquefaction, but also gain some insight regarding the effects of liquefaction. For instance, it could be useful in augmenting the procedure for calculating the 'Liquefaction Potential Index' (LPI), as defined by Iwasaki et al [38]. LPI is used in estimating the severity of liquefaction manifestation at the ground surface. A modification could be foreseen where a higher weight could be used while calculating LPI, if the site in question is susceptible to flow liquefaction. This would result in a higher value of LPI, which would imply a greater severity of liquefaction manifestation at the ground surface.

In summary, the overlying objective of this paper was to take another step towards bridging the gap between physics and empiricism when it comes to using liquefaction charts. The work presented in this paper represents an important step towards integrating the states of art and practice.

Chapter 4

EFFECT OF FABRIC ON SHEAR WAVE VELOCITY IN GRANULAR MATERIALS

[1] U. Mital, R.Y. Kawamoto, and J.E. Andrade. “Effect of fabric on shear wave velocity in granular materials”. submitted. 2016.

4.1 Introduction

The small-strain elastic shear wave velocity (V_S) is a basic mechanical property of soils and is an important parameter in geotechnical engineering. Together with the results of standard and cone penetration tests, it helps model the response of geomaterials to dynamic loading processes such as earthquakes and vibrations. Recently, V_S has been adopted as one of the indices (in addition to penetration resistance) for development of liquefaction charts [5, 34, 88]. Liquefaction charts are developed using the “simplified procedure” and are used to evaluate liquefaction resistance of soils in earthquake-prone regions [71].

The use of V_S as an index to quantify liquefaction resistance is based on the fact that both V_S and liquefaction resistance are similarly affected by many of the same parameters (such as void ratio, stress state, stress history and geologic age) [5]. Therefore, an understanding of how such parameters affect V_S helps in understanding the effect of such parameters on liquefaction resistance of soils. For instance, the effect of parameters such as relative density, stress state, and geologic age on soil resistance indices such as V_S are accounted for, and consequently their effects are incorporated in the evaluation of liquefaction resistance [34, 88]. Another important parameter whose effect is widely acknowledged to have a significant influence on liquefaction resistance is grain arrangement, or fabric [34]. Experiments have shown that the method of sample preparation, or the depositional environment, can significantly affect soil fabric and cause soils with the same stress states and relative densities to behave differently [46, 47, 62]. In fact, the effect of fabric has been established as a major concern when it comes to testing field samples in the laboratory, on account of sampling disturbance destroying the grain fabric. Quantification of in-situ fabric is still an open problem, and hence considerable judgement is needed in order to map laboratory test results to field conditions.

Given the effect of fabric on liquefaction resistance, it seems reasonable to expect that fabric also affects V_S. Indeed, Stokoe et al [75] proposed empirical correlations relating V_S to confining stresses where the proportionality constant is believed to be a function of soil fabric. Micro-mechanical studies have also been conducted that explore the effect of soil structure or fabric on small-strain shear modulus $G_{\max}$, which is proportional to V_S [1, 63, 89]. Such studies are important in order to quantify the effect of fabric while assessing liquefaction resistance.

In this paper, we conduct numerical simulations to investigate the effect of fabric on shear wave velocity (V_S) of soils. We use the 'level set discrete element method' (LS-DEM) [39, 41] and show that two granular assemblies, with the same stress state and void ratio but different fabric, can exhibit different liquefaction behavior. Subsequently, via a numerical implementation of the bender element test [49, 64, 74], we also obtain different V_S estimates for the two assemblies. Our results suggest how fabric can affect both liquefaction behavior and V_S of a granular assembly, suggesting that V_S can act as a proxy to account for the fabric effect while evaluating liquefaction resistance. We observe a possible correlation between fabric anisotropy and V_S anisotropy, quantification of which could imply that a knowledge of V_S anisotropy in the field would give us insight regarding the micro-mechanical structure of in-situ soil. For laboratory testing or simulation of soils, this could help in selection or development of a sample preparation technique that yields a similar V_S anisotropy as that in the field. Furthermore, a comparison of in-situ fabric and laboratory fabric could aid researchers in more accurately mapping laboratory or simulation results to field conditions.

4.2 Simulation Methodology

Our numerical investigation was conducted using the 'level set discrete element method' (LS-DEM) [39, 41]. LS-DEM is a variant of the discrete element method (DEM), which is a numerical method that describes the mechanics of an assembly of particles [17]. LS-DEM enables an accurate depiction of irregular particle shapes using level sets. In this work, we used a 2D level set representation of caicos ooid grains as obtained by Lim et al [52], following the characterization methodology proposed by Vlahinic et al [83]. The caicos ooid grains were obtained in dimensions of pixels. These were rescaled assuming a pixel size of 0.1095^2 mm^2, yielding a mean grain area of 5.4 mm^2. Thickness of grains was assumed to be 1 pixel length. Table 4.1 outlines the values of model parameters used in the LS-DEM model. Our time step was equal to 1.36 μs, which is smaller than the critical time step required for stable DEM analysis [77].

Table 4.1: Model parameters and values used in the LSDEM model

Model parameters	Values
Inter-particle friction	0.3
Wall friction	0
Normal contact stiffness (Particle and wall)	2.74×10^8 N/m
Particle shear contact stiffness	2.47×10^8 N/m
Particle density	2.7×10^3 kg/m^3
Global damping	5×10^3 s^{-1}
Contact damping	0
Time step	1.36×10^{-6} s

Fabric quantification

We quantified fabric using the classic 2nd order fabric tensor based on contact normals [40]:

$$F_{ij} = \frac{1}{N}\sum_{c=1}^{N} n_i^c n_j^c \tag{4.1}$$

where n_i^c is the $i-$th component of contact normal at contact c. The fabric anisotropy A is defined as:

$$A = 2(F_1 - F_2) \tag{4.2}$$

where F_1 and F_2 are the major and minor principal values, respectively, of the fabric tensor. The orientation (θ_F) of F_1 may be used to define the orientation of fabric anisotropy A. We can use a 2nd order Fourier expansion to obtain the probability density $P(\theta)$ of contact normals [12]:

$$P(\theta) = \frac{1}{2\pi}\{1 + A\cos 2(\theta - \theta_F)\} \tag{4.3}$$

where θ is the orientation of a contact normal. A perfectly isotropic fabric will be circular in polar coordinates, whereas an anisotropic fabric will tend towards a ‘peanut’ shape.

There are many different ways to quantify fabric. Kuhn et al [45] provides a good review. The anisotropic stiffness of a granular assembly is inherently linked to the directionality of force chains. Therefore, choosing contact normals as a basis for fabric quantification seems justified.

Granular assembly generation

Our objective here was to obtain two granular assemblies with similar stress states and void ratio but different fabric. Figure 4.1 summarizes our methodology to obtain an initial assembly. Computational limitations necessitated the use of an unconventional approach to assembly generation. An initial assembly of 800 grains was first developed (explained below) which was duplicated and placed in a 2x2 grid, resulting in 3200 grains. This resulted in clear interfaces visible at the boundaries of the individual 800 grain assemblies. To remove the interfaces, the assembly was first isotropically consolidated to 100 kPa, then a central bin of grains was perturbed at an angle of 45 degrees. The inter-particle friction was then temporarily turned off, and the assembly allowed to relax, resulting in a stress-free assembly with grains densely packed together. The inter-particle friction was turned back on and the assembly was isotropically consolidated to 100 kPa.

To obtain the 800 grain assembly, grains were placed in a hexagonal packing such that no two particles were in contact with each other. The aspect ratio of the packing was approximately 1:2, with the approximate dimensions being 5 cm $\times$ 10 cm. The assembly was then isotropically consolidated to 5 MPa, then unloaded to 100 kPa, and then subjected to constant volume biaxial loading to change the aspect ratio to 1:1. The resultant assembly had a predominantly vertical fabric (not shown). The inter-particle friction was then temporarily turned off, and the assembly allowed to relax, resulting in a stress-free assembly with grains densely packed together. This assembly was then duplicated to generate the 3200 grain assembly (as described above).

The resultant 3200 grain assembly, isotropically consolidated to 100 kPa, was then subjected to two different loading histories, in order to generate two assemblies with similar stress states and void ratio, but different fabric anisotropy. The initial fabric of the assembly is shown in Figure 4.2. We refer to the two assemblies as ‘assembly 1’ and ‘assembly 2’. The loading history for assembly 1 involved simple shear loading, sheared to an angle of 20 degrees, and subsequently sheared back to 0 degrees. This gave the assembly a pronounced diagonal anisotropy (Figure 4.2),

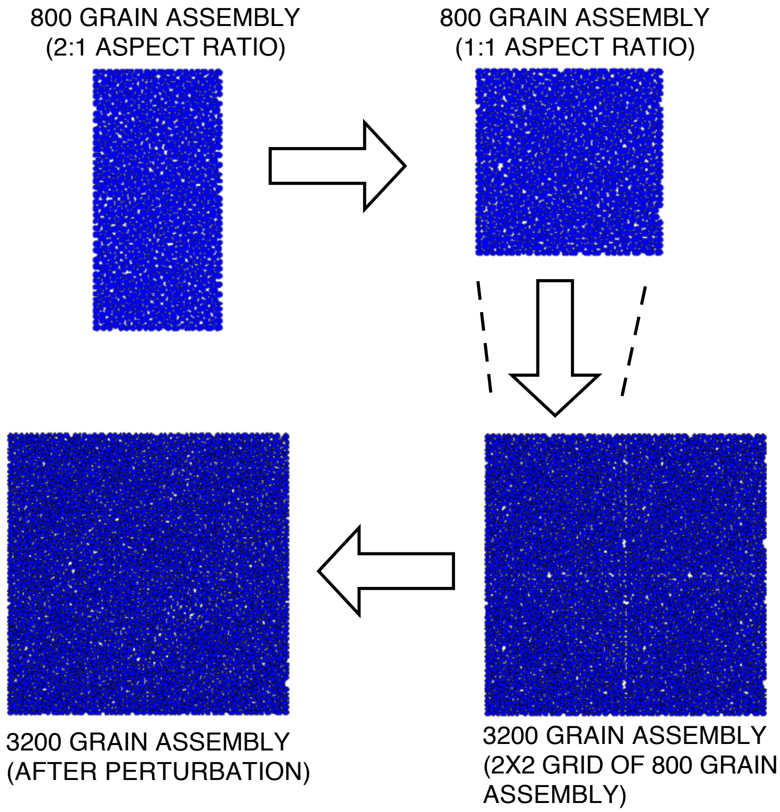

Figure 4.1: Initial assembly generation

with the fabric oriented at an angle of 34 degrees clockwise with the vertical. The assembly had a resultant void ratio of $e = 0.17$, and a stress state of $p = 85$ kPa, and $q = 30$ kPa. Here, $p = (\sigma_1 + \sigma_2)/2$ is the volumetric stress (or pressure), and $q = \sqrt{(\sigma_2 - \sigma_1)^2 + 2\sigma_{12}^2}$ is the deviatoric stress. σ_1 is the lateral stress, σ_2 is the axial stress, and σ_{12} is the shear stress.

The loading history for assembly 2 involved two stages of loading to match the stress state of the first assembly. First stage was isotropic unloading, and second stage was axial loading at constant lateral stress, resulting in the same p and q as assembly 1. The fabric anisotropy of the second assembly was predominantly vertical, oriented at an angle of 5 degrees counter-clockwise with the vertical. This was very similar to the initial assembly, oriented at an angle of 7 degrees counter-clockwise with the vertical (Figure 4.2). The assembly had a resultant void ratio of $e = 0.15$ (which is very similar to the void ratio of assembly 1).

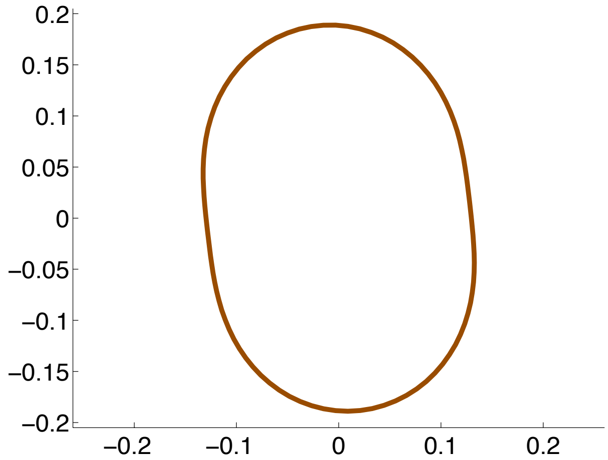

(a)

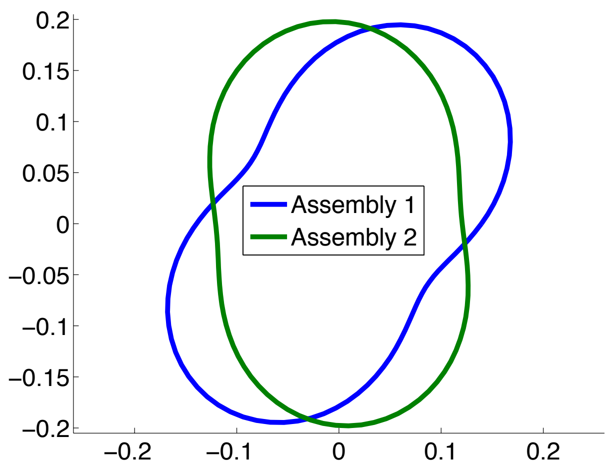

(b)

Figure 4.2: Fabric anisotropies of different assemblies. (a) Initial assembly with A = 0.19, θ_F = -7 degrees. (b) Assembly 1 with A = 0.34, θ_F = 34 degrees, Assembly 2 with A = 0.25, θ_F = -5 degrees. Here A is fabric anisotropy and θ_F is fabric orientation measured clockwise from the vertical, as defined in section 4.2.

4.3 Liquefaction behavior

Liquefaction behavior is associated with undrained, or constant volume loading. Here, the assemblies were subjected to biaxial loading, with axial compression under constant volume constraint. Results are shown in Figure 4.3. Assembly 2, whose fabric anisotropy is largely aligned with the direction of axial compression (vertical) shows stable strain-hardening behavior. However, assembly 1, whose fabric anisotropy is oriented at angle of 34 degrees to the vertical, shows extensive strain-softening associated with liquefaction behavior. Figure 4.3 clearly demonstrates how two assemblies with the same stress state and void ratio can exhibit different behavior if their fabric is different.

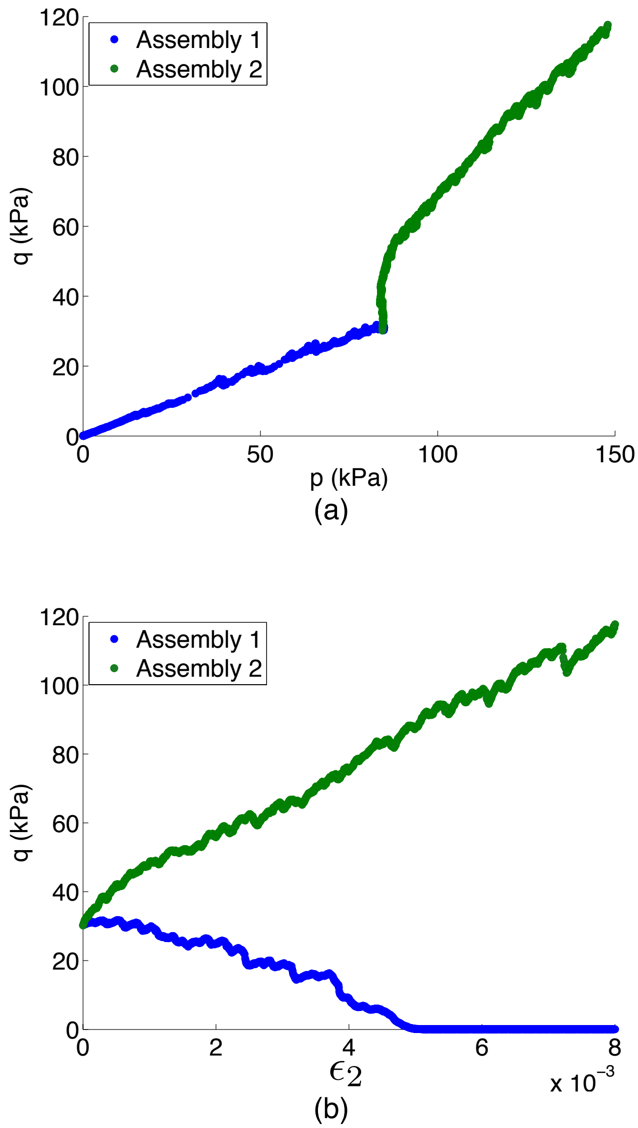

Figure 4.3: Liquefaction behavior results. (a) deviatoric stress (q) vs volumetric stress (p). (b) deviatoric stress (q) vs axial strain (ϵ_2). Assembly 1 exhibits extensive strain-softening associated with liquefaction behavior, whereas assembly 2 shows stable strain-hardening behavior.

The high strength of assembly 2 is expected in light of contact orientations as visualized in Figure 4.2. A high contact anisotropy in the direction of loading facilitates load transmission through the granular assembly, and makes the assembly more dilatant. [50, 67].

4.4 Shear velocity estimation

Having seen the two assemblies show distinct liquefaction behaviors, we now seek to estimate the small-strain shear velocities of the two assemblies. From the prevalent understanding of V_S-based liquefaction correlations, we expect assembly 2 to have a higher vertical V_S than the assembly 1.

Different approaches exist to estimate the shear velocity or shear modulus of a granular assembly. From a theoretical standpoint, early investigations studied the behavior of two equal spheres pressed together by a normal force and then subjected to a shearing force [56, 57]. Subsequent theoretical investigations considered an aggregate of equal spheres in a cubic packing [23] and in a face-centered cubic lattice [26]. Experiments on a rod of steel spheres [26] demonstrated that shear velocity predictions obtained from theories of perfect spheres can not be expected to agree closely with experiments on real granular soils. Early experimental investigations to study wave propagation in sands involved the 'resonant-column test' [30, 35]. This test subjected a vertical column of sand to longitudinal or torsional oscillations. More recently, an alternate experimental technique called the 'bender element test' [49, 74] was developed. Over the years, the bender element test has gained popularity owing to its simplicity and ease of use, and has also been implemented numerically using the discrete element method [54, 64, 65]. This makes the numerical bender element test an excellent candidate to estimate shear velocities in our granular assemblies.

Numerical bender element test

The bender element test consists of a transmitter element that generates a shear wave, and a receiver element that detects the transmitted disturbance. We chose a bin of particles as the transmitter element. In simulations, as opposed to experiments, it is possible to know the displacement of each particle. Therefore, instead of having a single particle act as a receiver, we tracked the shear displacement for a central column of grains (away from the boundaries) along the entire length of the assembly (denoted by grains colored with a black to white gradient in Figure 4.4). This simplified the analysis as it became convenient to identify shear waves. The assembly was discretized into bins with approximate dimensions 40×40 pixels, or 4.4 $\times$ 4.4 mm^2. We plotted two-dimensional contours of the central column of particle displacements along the direction of propagation. In the contour plot, the zero crossings of the received signals were clearly visible as a distinct contour line. The average slope of this line was then taken as the shear wave velocity [65]. Figure 4.5 shows the bender element test results for an 800 grain assembly, isotropically consolidated to 50 kPa. The transmitter bin was the bottom-most bin of the central column. The slope of the zero contour line yielded a shear velocity estimate of V_S = 202 m/s.

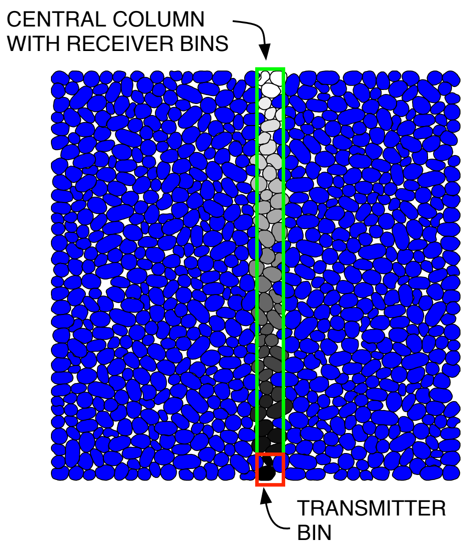

Figure 4.4: Illustration of how shear displacement is tracked for a central column of grains. The central column is denoted by grains that are colored with a black to white gradient.

We used a square wave input with a rise time of 100 time steps and amplitude of 1 pixel. A square wave is a robust input signal that contains all the frequencies [49]. A drawback of the square wave is that the system response necessarily exhibits a 'near-field' effect due to faster moving compressional waves [68]. As a result, it is often not straightforward to determine the arrival of the shear wave. Although the point of first inflection is sometimes considered to be a fair estimate of shear wave arrival [82], research suggests that the arrival of the shear wave does not correspond to a distinctive point in the signal [54]. Various signal interpretation techniques exist to aid in estimating shear wave velocity in an experimental bender element test[65, 87]. For our purpose, since we have access to displacement of each particle, we tracked the shear displacement for a central column of grains along the

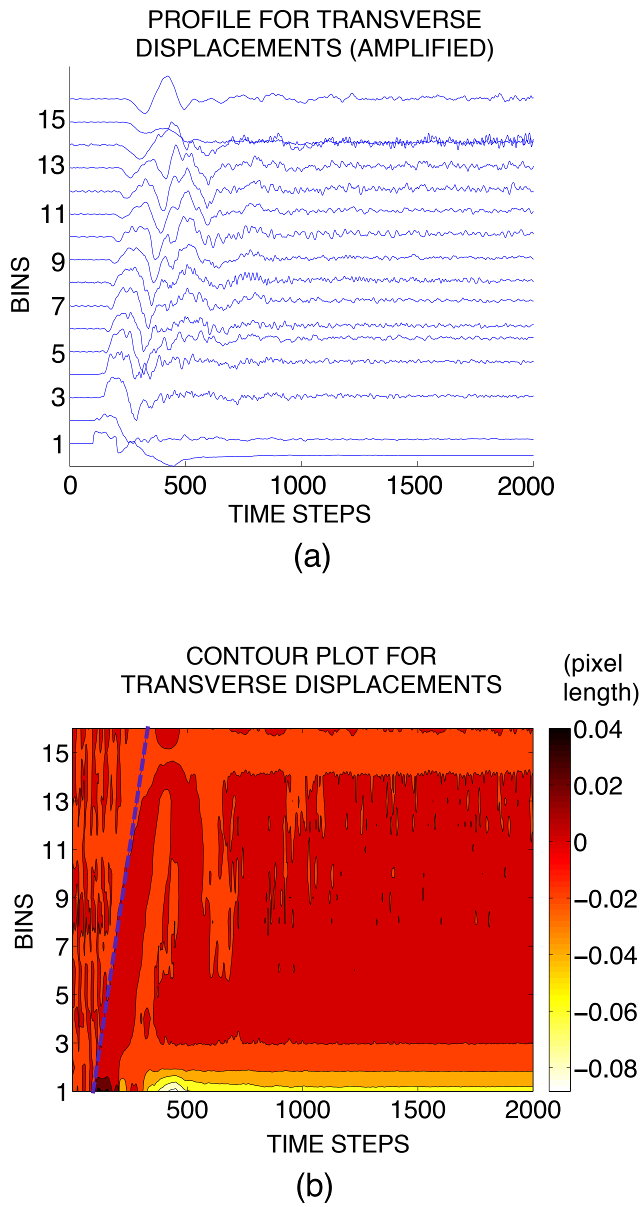

Figure 4.5: Shear velocity estimate for the assembly in Figure 4.4. The blue line in the contour plot in (b) is the average slope estimate for the zero crossing of the received signal, yielding V_S = 202 m/s. 1 bin ≈ 40 × 40 pixels, 1 pixel length = 0.1095 mm, 1 time step = 1.36 μs.

entire length of the assembly. Note that the area on the contour plot between the initial noise and the zero contour line corresponds to the near field effect.

Verification exercise

In order to verify our implementation of the bender element test, we also estimated the shear wave velocity V_S by calculating $G_{\max}$ in a biaxial test. The two quantities are related as:

$$V_S = \sqrt{\frac{G_{\max}}{\rho}} \tag{4.4}$$

where ρ is the density of the granular assembly. To measure $G_{\max}$, an assembly in an isotropic stress state can be subjected to an axial strain of 10^{-4}. This value of strain coincides with the value of 'threshold strain', as defined by Dobry et al [25]. The threshold strain is the strain value till which all the deformations in the granular assembly can be assumed to be elastic. In our 3200 grain assembly, isotropic consolidation also resulted in shear stresses on the walls, typically of the order of about 1% of the confining pressure. Such a small amount of shear stress was sufficient to generate non-linear stress-strain curves, which disabled the approximation of elastic constants. Therefore, we resorted to the smaller 800 grain assembly, prepared as described in section 4.2. When the smaller assembly was consolidated to a pressure of 50 kPa, shear stresses on the wall were negligible ($\sim$ 0.2% of confining pressure). Axial loading to threshold strain yielded a linear stress-strain curve (Figure 4.6), making it suitable for computing $G_{\max}$, and consequently V_S, enabling a comparison with the V_S estimate obtained in Figure 4.5.

Following the approach by O'Donovan et al [64], we conducted a biaxial stress at constant lateral stress, till an axial strain of 10^{-4} was achieved. As shown in Figure 4.6, the plot of deviator stress q vs axial strain ϵ_2 is a straight line. The slope of the plot, which is within the limit of threshold strain, yields the elastic Young's Modulus E:

$$E = \frac{dq}{d\epsilon_2} = 237 \text{ MPa} \tag{4.5}$$

where dq is the increment in deviatoric stress, and $d\epsilon_2$ is the increment in axial strain. Note that deviatoric stress $q = \sigma_2 - \sigma_1$. Furthermore, by monitoring the lateral strain ϵ_1, we also obtained the poisson's ratio ν, as shown in Figure 4.6:

$$\nu = \frac{-d\epsilon_1}{d\epsilon_2} = 0.21 \tag{4.6}$$

where $d\epsilon_1$ is the increment in lateral strain. $G_{\max}$ was then calculated as:

$$G_{\max} = \frac{E}{2(1+\nu)} = 97.9 \text{ MPa} \tag{4.7}$$

To obtain V_S, we need the density ρ of the granular assembly, which was calculated as:

$$\rho = \frac{\rho_{\text{grains}} \times A_{\text{grains}}}{A_{\text{tot}}} = 2.33 \times 10^3 \text{ kg/m}^3 \tag{4.8}$$

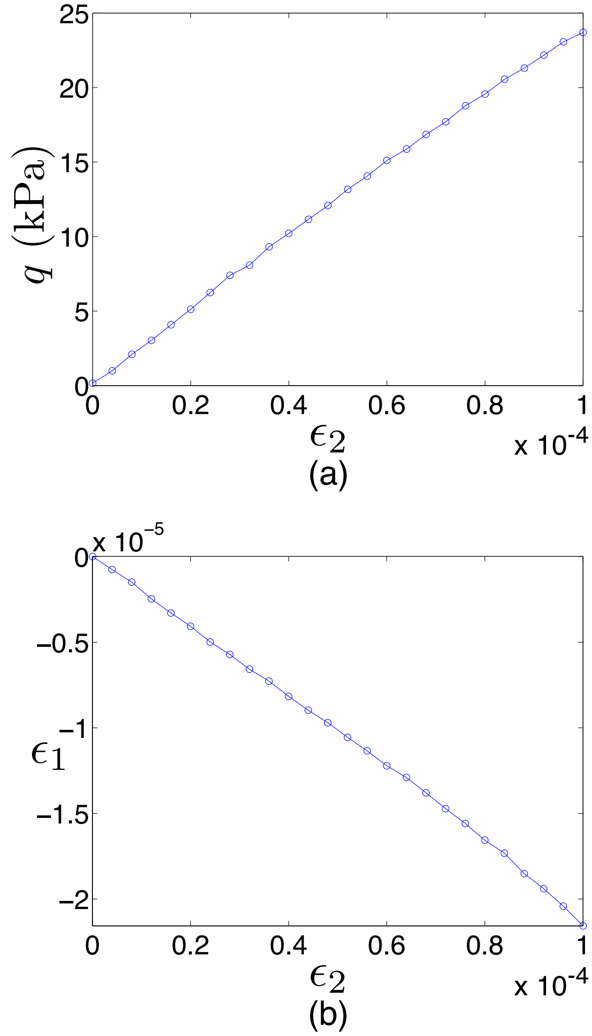

Figure 4.6: Biaxial test at constant lateral stress for the 800 grain assembly, up to an axial strain corresponding to threshold value of 10^{-4}. (a) deviator stress vs axial strain, yielding an elastic Young's modulus of 237 MPa. (b) Lateral strain vs axial strain, yielding a poisson's ratio of 0.21.

where $\rho_{\text{grains}} = 2.7 \times 10^3$ kg/m^3 is the density of grains as specified in Table 4.1, $A_{\text{grains}} = 4.3 \times 10^3$ mm^2 is the total area of grains in the assembly, and $A_{\text{tot}} = 4.99 \times 10^3$ mm^2 is the total area of the assembly. Finally using equation 4.4, the shear velocity was found to be V_S = 205 m/s, which is in good agreement with the V_S estimate obtained in Figure 4.5.

Shear Velocity results

Once verified, we used the numerical bender element test technique to obtain V_S estimates for the two 3200 grain assemblies. The assemblies were discretized into bins with similar dimensions as those specified in Figure 4.5, and the transmitter bin was perturbed horizontally with a square input wave, that had the same rise time and amplitude as in the 800 grain example used for verification. Since V_S is a proxy for liquefaction resistance, it is reasonable to expect that in the vertical direction, assembly 1, which showed extensive strain-softening associated with liquefaction, should have a lower vertical V_S than assembly 2, which exhibited stable strain-hardening behavior. We consider V_S in the vertical direction since that is the direction in which the two assemblies were subjected to axial compression. Subsequently, we also estimate V_S in different directions to investigate the correlation of anisotropy of V_S with the fabric.

Figure 4.7 shows contour plots with average slope estimates, for the 3200 grain assembly 1 and 3200 grain assembly 2. For these plots, the transmitter bin was not the bottom-most bin of the central column. Different locations of the transmitter bin along the central column yielded slightly different V_S estimates, owing to the inherent heterogeneity of the assembly. Therefore, multiple tests (at least three) were simulated with transmitter bins placed at different locations along the central column in order to obtain statistical estimates of V_S.

It is possible that our technique of assembly generation induced significant heterogeneities in the grain fabric. For certain tests, contour plots did not yield distinct contour lines corresponding to zero crossing. Figure 4.8 shows one such test, where there is a high signal dissipation resulting in the lack of a distinct contour line beyond the first few receiver bins. A distinct contour line is necessary in order to estimate its average slope, and consequently V_S. While estimating the slope, we considered a subset of the contour line to ensure that the average slope line (dashed blue line in Figures 4.5 and 4.7) passes the transmitter bin near the time step corresponding to initiation of the input wave.

Table 4.2 shows the test results for V_S in the vertical direction for assemblies 1 and 2, along with the computed mean values. The paucity of results for assembly 1 is due to the fact that a lot of tests produced contour plots similar to those in Figure 4.8, and were unable to yield V_S estimates. The statistics show that on average, estimates of vertical V_S for assembly 2 are higher than those of assembly 1. Table 4.2 clearly shows that the difference in liquefaction resistance of assemblies 1 and

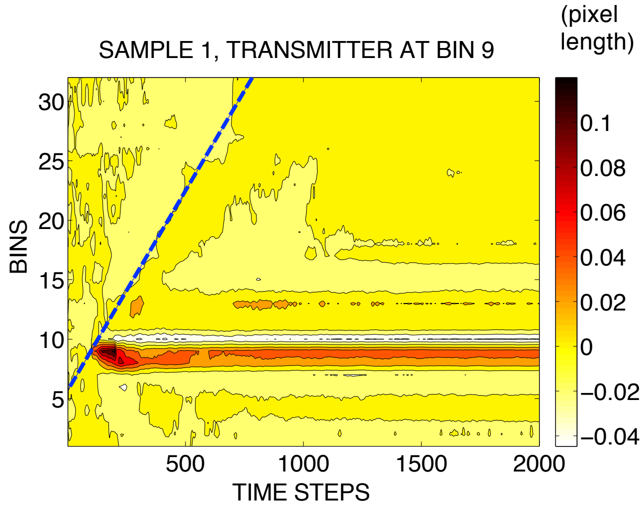

(a)

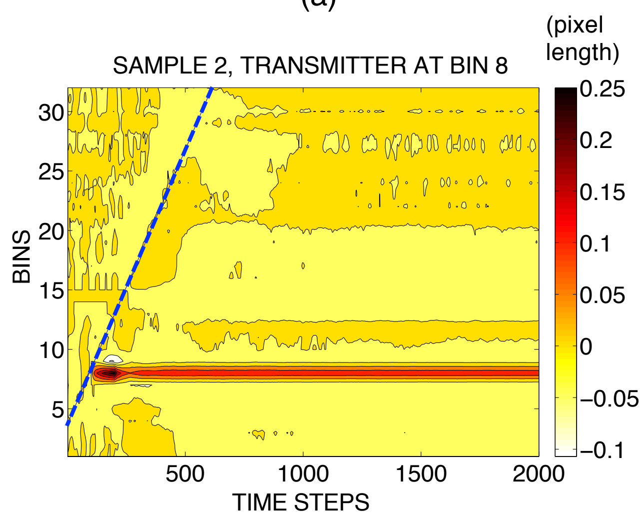

(b)

Figure 4.7: Contour plots for transverse displacement. (a) assembly 1. (b) assembly 2. The dashed blue line on the plots is the average slope estimate for the zero crossing of the received signal, which yields a V_S estimate (110 m/s for assembly 1 and 148 m/s for assembly 2). 1 bin $\approx 40 \times 40$ pixels, 1 pixel length = 0.1095 mm, 1 time step = 1.36 μs.

2 (as shown in Figure 4.3), is also accompanied by a difference in their vertical V_S. The assembly that is resistant to liquefaction shows a higher vertical V_S, something that is also expected from the current understanding of V_S-based liquefaction correlations [34, 88].

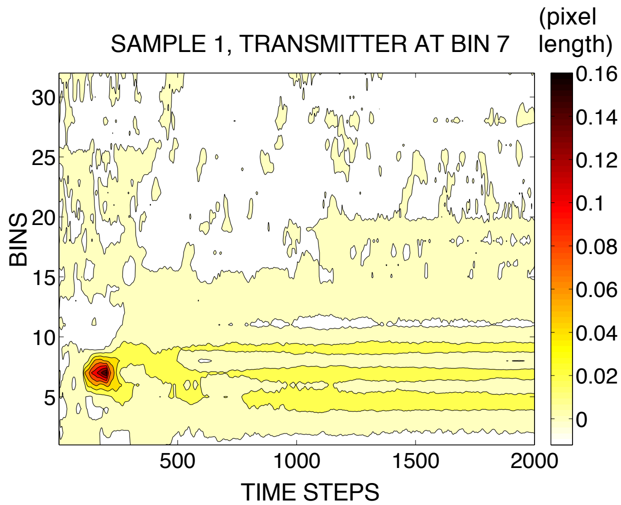

Figure 4.8: Contour plot for transverse displacement, for assembly 1 with transmitter at bin 7. Note the high signal dissipation and the lack of a distinct contour line beyond the first few receiver bins, which disables a V_S estimation. 1 bin $\approx 40 \times 40$ pixels, 1 pixel length = 0.1095 mm, 1 time step = 1.36 μs.

Table 4.2: Test results for V_S in the vertical direction for assemblies 1 and 2

Bin location (Transmitter)	Assembly 1 V_S (m/s)	Assembly 2 V_S (m/s)
1	-	113
2	-	-
3	115	-
4	-	-
5	-	-
6	-	122
7	-	-
8	-	148
9	110	142
10	105	136
11	-	126
Mean	110	131

Correlation of V_S anisotropy with fabric anisotropy

In addition to obtaining estimates for vertical V_S for assemblies 1 and 2, we also obtained estimates for V_S in different directions. This was done to investigate a possible correlation between anisotropy of shear-stiffness or V_S and fabric anisotropy. We conducted an ‘angle sweep’, i.e., we conducted tests where the transmitter bin was sheared at an angle to the horizontal to transmit a shear wave at an angle.

Figure 4.9 illustrates one such test configuration. The central column (denoted by grains with a black to white gradient) which acted as the receiver was inclined, or rotated, at the same angle with the vertical. Furthermore, the transmitter bin was placed away from the boundaries to prevent wave reflections from corrupting the test results. As observed for vertical V_S estimates, different locations of the transmitter bin along the central column yielded slightly different V_S estimates, owing to the inherent heterogeneity of the assembly. Therefore, multiple tests (at least three) were simulated with the transmitter bin placed at different locations along the central column to obtain statistical estimates of V_S. As with the vertical V_S tests, not all tests yielded contour plots with distinct contour lines corresponding to zero crossing. For the 'angle sweep', the inclination angle θ of the central column was varied from $(-90, 90]$ degrees, in increments of 30 degrees. The angle is positive when measured clockwise from the vertical. This yielded V_S estimates for the entire rotation of 360 degrees since the central column is the same for rotation of θ and $\theta + 90$ (degrees). Figure 4.10 shows the results of the 'angle sweep' for assemblies 1 and 2.

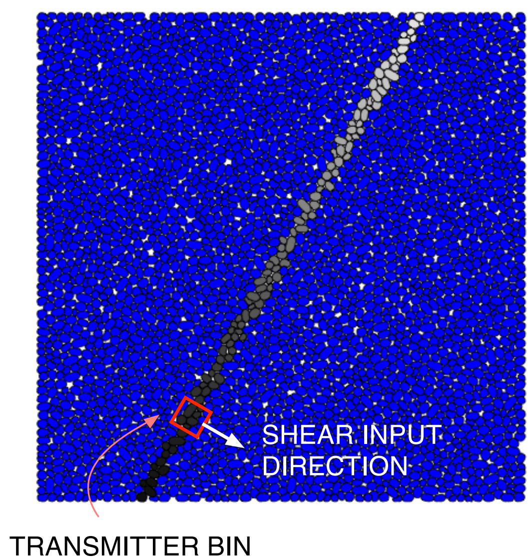

Figure 4.9: Illustration of how V_S estimates are obtained in different directions. The central column (denoted by grains that are colored with a black to white gradient) is rotated at a desired angle with the vertical. The transmitter bin is located in the central column and is sheared perpendicular to the inclination of the central column.

A comparison of anisotropic V_S estimates for assembly 1 (Figure 4.10a) with its fabric anisotropy (Figure 4.2b) suggests a strong influence of contact anisotropy on V_S. Assembly 1 has the majority of contacts aligned at angle of 34 degrees from

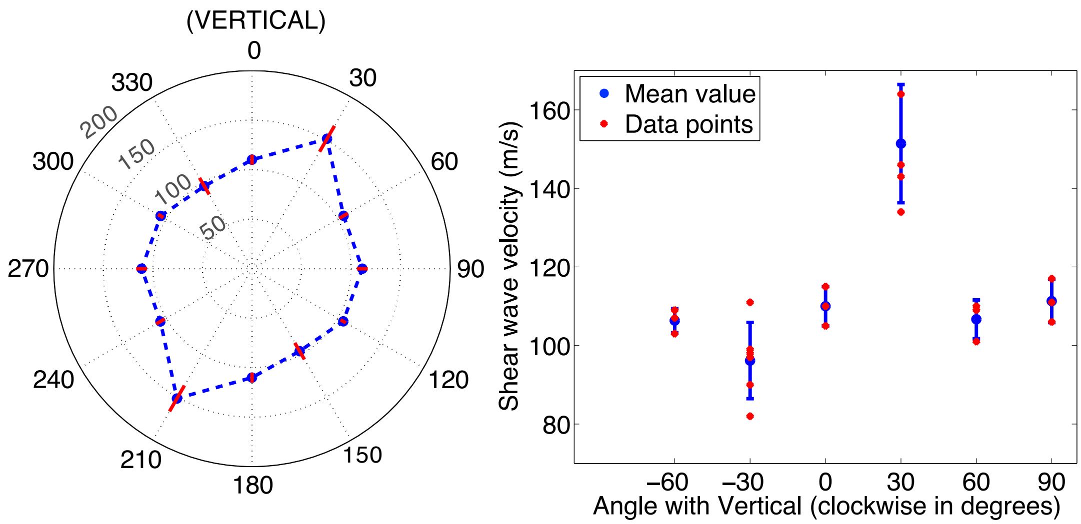

(a) Assembly 1

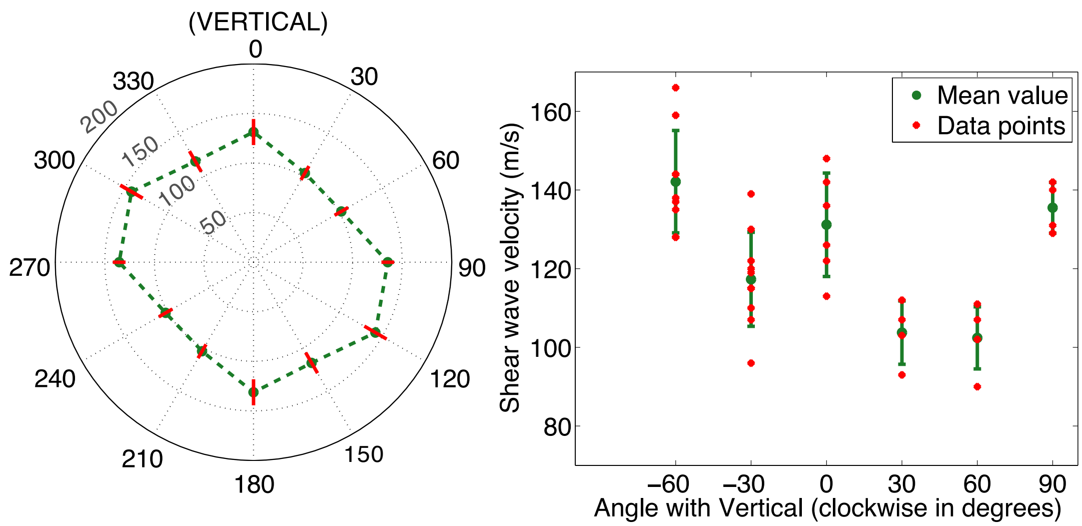

(b) Assembly 2

Figure 4.10: Results of V_S 'angle sweep', giving estimates of V_S in different directions. (a) Assembly 1, (b) Assembly 2. Left: Polar plot with the radius corresponding to V_S, and angle corresponding to angle with vertical (clockwise). Right: Linear plot of V_S vs angle with vertical. The error bars correspond to one standard deviation.

the vertical, and also has the highest V_S in the corresponding orientation, suggesting a strong dependence of shear-stiffness on contact normals. This is not surprising, since the assembly was subjected to simple shear loading (section 4.2), causing the contacts to preferentially align along the principal direction of loading.

The anisotropic V_S estimates for assembly 2 (Figure 4.10b) do not seem to correlate well with its fabric anisotropy (Figure 4.2b). There is an anomalous peak in V_S at a direction of 60 degrees counter-clockwise from the vertical. While a detailed investigation of this anomaly is beyond the scope of current work, a cursory investigation suggests a plausible answer. Firstly, it may be noted from Figure 4.2 that while generating assembly 2, the change in fabric from the initial configuration was minimal. Therefore, as opposed to assembly 1, assembly 2 did not experience large-scale destruction and creation of contacts. Secondly, we investigated the fabric anisotropy of increasingly strong contacts. A strong contact is one whose contact force is higher than the mean contact force of the assembly [12]. Interestingly, for the initial assembly, the fabric anisotropy of the ten strongest contacts was largely aligned with the horizontal (Figure 4.11a). Furthermore, the fabric anisotropy of the 10 strongest contacts for assembly 2 was aligned at about 20 degrees counter-clockwise from the vertical (Figure 4.11b). Such anomalous orientation of the strongest contacts was not prevalent in assembly 1 (not shown). This suggests the possibility of assembly 2 having contacts with high compressive forces along the horizontal axis as well as along 60 degrees counter-clockwise from the vertical, which contributed to the high stiffness and consequently high V_S estimates in those directions. Since our fabric quantification did not account for the magnitude of contact forces, the aforementioned contacts were averaged out. It is possible that a more sophisticated fabric estimate that can better capture this effect.

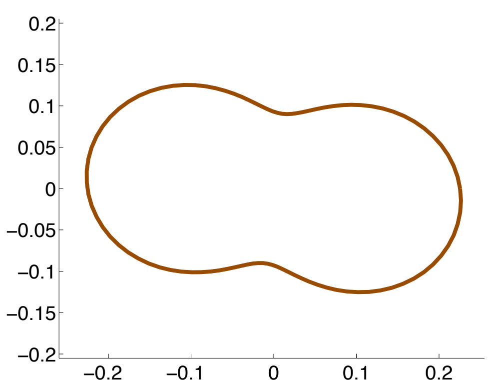

(a)

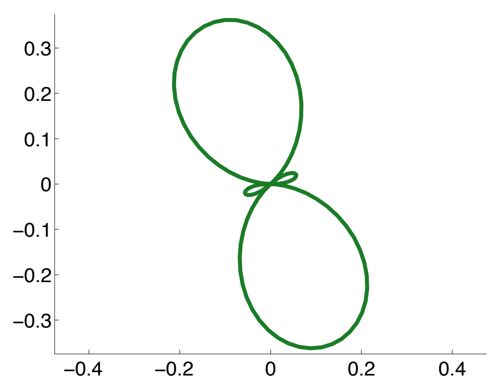

(b)

Figure 4.11: Fabric anisotropies of the ten strongest contacts. (a) Initial assembly with A = 0.43, θ_F = 97 degrees. (b) Assembly 2 with A = 1.38, θ_F = -20 degrees. The small lobe perpendicular to the main lobe is a numerical artifact caused by using the Fourier fit as defined in equation 4.3. Here A is fabric anisotropy and θ_F is fabric orientation measured clockwise from the vertical, as defined in section 4.2.

4.5 Conclusions

Figure 4.3 shows that the two 3200 grain assemblies behave differently under constant volume biaxial compression. Table 4.2 shows that the two assemblies also have different vertical V_S estimates, with the strain-hardening assembly having a higher vertical V_S than the strain-softening assembly. In addition, Figure 4.10 shows that the two assemblies also yield distinct anisotropic estimates of V_S. Although there is some uncertainty in measurements of V_S, the trends are clear. Both assemblies have the same initial stress state characterized by the volumetric stress p, deviatoric stress q, as well as a similar void ratio e. The only difference is fabric, which we quantify on the basis of contact normals. This suggests that while assessing liquefaction potential in the field, V_S might serve as a suitable proxy to estimate not just the prevailing stress state and relative density, but also the prevailing soil fabric. Our results suggest the existence of a correlation between V_S anisotropy and fabric anisotropy—a correlation that can be explored with more detailed micro-mechanical investigations. Such investigations may benefit by the use of periodic boundary conditions. Results of such future investigations could imply that a knowledge of V_S anisotropy in the field would give us insight regarding the micro-mechanical structure of in-situ soil. For lab testing or simulation of soils, this could help in selection or development of a sample preparation technique that yields a similar V_S anisotropy as that in the field. Furthermore, a comparison of in-situ fabric and laboratory fabric could aid researchers in more accurately mapping laboratory or simulation results to field conditions.

Chapter 5

CONCLUSIONS AND FUTURE OUTLOOK

This thesis presented some key developments regarding the micro and macro mechanics of soil liquefaction. These developments should facilitate a more physical assessment of liquefaction susceptibility at the field-scale.

The simplest manifestation of liquefaction occurs when a soil specimen is subjected to monotonic or static loading under undrained conditions in a triaxial compression test. By analyzing the mechanics underlying the onset of flow liquefaction in such a setting, we developed a fundamental understanding of the phenomenon. Specifically, we defined a flow liquefaction potential $\mathcal{L}$ that helped understand soil behavior under conditions of 'partial drainage'. Flow liquefaction potential $\mathcal{L}$ provides an elegant framework to visualize how a soil can liquefy despite volume changes prevalent under partial drainage; this can happen during seismic shaking in the field, or under static loading when there is differential pore pressure generation between adjacent soil layers with different densities. Unequal pore pressure generation can lead to pore water being injected into certain layers and being extracted from other layers, causing volume changes. In addition, by analyzing the evolution of stresses in a triaxial compression test, we were also able to identify a necessary precursor for the onset of flow liquefaction instability. The concept of a necessary precursor can help in identifying at-risk slopes in hydraulic fill dams, spoil tips, and tailings – slopes that are formed of loose deposits and are susceptible to flow liquefaction under undrained loading.

A numerical investigation into the mechanics of liquefaction charts revealed that the lower end of these charts may correspond to sites that are susceptible to flow liquefaction, as opposed to cyclic mobility. This could arm an engineer with some predictive power regarding the effects of liquefaction. For instance, it could be useful in augmenting the procedure for calculating the 'Liquefaction Potential Index' (LPI), as defined by Iwasaki et al [38]. LPI is used in estimating the severity of liquefaction manifestation at the ground surface. A modification could be foreseen where a higher weight could be used while calculating LPI, if the site in question is susceptible to flow liquefaction. This would result in a higher value of LPI, which would imply a greater severity of liquefaction manifestation at the ground surface.

A grain-scale numerical investigation enabled us to investigate the micro-mechanics of shear wave velocity in a granular assembly. Specifically, we observed how the anisotropy of fabric, or grain-arrangement, affects the shear wave anisotropy. The differences in fabric are also accompanied by a difference in liquefaction resistance of a granular assembly. This suggests that while assessing liquefaction potential in the field, shear velocity may serve as a suitable proxy to estimate not just the prevailing stress state and relative density – as is the case presently, but also for estimating the prevailing soil fabric. Our results suggest the existence of a correlation between shear wave anisotropy and fabric anisotropy, suggesting that knowledge of shear wave anisotropy could provide insight regarding the micro-mechanical structure of in-situ soils. Such knowledge could help in translating laboratory test results onto field conditions, with greater certainty, and consequently refine the field-assessment of liquefaction susceptibility.

5.1 Future Outlook

Some future research directions are immediately apparent from this thesis. For instance, we identified a necessary precursor prior to the onset of flow liquefaction in a triaxial compression test. This provides motivation to look for a necessary precursor at the field-scale. Knowledge of a precursor could be useful if slopes are fitted with instruments monitoring their deformation, or if slopes are monitored via remote sensing satellites. Once at-risk slopes are identified, steps could be taken to mitigate the effects of the liquefaction risk.

We also suggested a modification in the calculation of LPI wherein sites susceptible to flow liquefaction could be assigned a higher weight. Presently, when LPI is calculated at a site, all liquefaction occurrences are treated the same, with no distinction between flow liquefaction and cyclic mobility. Empirical limits based on existing liquefaction case histories are used to determine whether an LPI value corresponds to significant liquefaction hazard at the surface. However, these empirical limits have been found to vary depending on the location of the hazard [55]. Is it possible for the LPI values to have more uniformity across regions, if we incorporate for the different effects of flow liquefaction and cyclic mobility? Chapter 3 of this thesis gives us motivation to explore this question.

The results in Chapter 4 suggest a correlation between shear wave anisotropy and fabric anisotropy. This motivates a detailed micro-mechanical study to explore such a correlation, so that knowledge of shear wave anisotropy in the laboratory or the field can be used to reliably quantify the soil fabric. A numerical study via the discrete element method seems the most plausible path, since numerical simulations permit investigation of grain-scale properties and can be used to develop an appropriate fabric quantification. Any correlation proposed via numerical studies must be subsequently validated via laboratory investigations before it can be tested in the field.

5.2 Closing Remarks

A more fundamental understanding of the physics of soil liquefaction can aid in the development of liquefaction hazard maps, which map entire regions and help identify areas where liquefaction is likely to occur. Development of such maps is a necessary endeavor to make cities and economies resilient to the effects of liquefaction. By investigating the micro and macro mechanics, this thesis helps in a more physical assessment of liquefaction susceptibility and its accompanying hazards, at the field-scale and the regional scale.

BIBLIOGRAPHY

[1] I. Agnolin and J.N. Roux. "Internal states of model isotropic granular packings. III. Elastic properties". In: *Physical Review E* 76.6 (2007), p. 061304.

[2] A. Alarcon-Guzman, G.A. Leonards, and J.L. Chameau. "Undrained monotonic and cyclic strength of sands". In: *Journal of Geotechnical Engineering* 114.10 (1988), pp. 1089–1109.

[3] J.E. Andrade. "A predictive framework for liquefaction instability". In: *Géotechnique* 59.8 (2009), pp. 673–682.

[4] J.E. Andrade, A.M. Ramos, and A. Lizcano. "Criterion for flow liquefaction instability". In: *Acta Geotechnica* 8.5 (2013), pp. 525–535.

[5] R. D. Andrus and K. H. Stokoe II. "Liquefaction resistance of soils from shear-wave velocity". In: *Journal of Geotechnical and Geoenvironmental Engineering* (2000).

[6] R.D. Andrus et al. "Comparing liquefaction evaluation methods using penetration-V_S relationships". In: *Soil Dynamics and Earthquake Engineering* 24.9 (2004), pp. 713–721.

[7] K. Been and Mike G. Jefferies. "A state parameter for sands". In: *Géotechnique* 35.2 (1985), pp. 99–112.

[8] A.W. Bishop. "The stability of tips and spoil heaps". In: *Quarterly Journal of Engineering Geology and Hydrogeology* 6.3-4 (1973), pp. 335–376.

[9] R.W. Boulanger. "High overburden stress effects in liquefaction analyses". In: *Journal of Geotechnical and Geoenvironmental Engineering* 129.12 (2003), pp. 1071–1082.

[10] R.W. Boulanger. "Relating K_α to relative state parameter index". In: *Journal of Geotechnical and Geoenvironmental Engineering* 129.8 (2003), pp. 770–773.

[11] R.W. Boulanger and R.B. Seed. "Liquefaction of sand under bidirectional monotonic and cyclic loading". In: *Journal of Geotechnical Engineering* 121.12 (1995), pp. 870–878.

[12] B. Cambou, M. Jean, and F. Radjai. *Micromechanics of granular materials*. John Wiley & Sons, 2013.

[13] G. Castro. "Liquefaction of sands, Harvard soil mechanics series 81". In: *Cambridge, MA: Harvard University* (1969).

[14] J.C. Chern. "Undrained response of saturated sands with emphasis on liquefaction and cyclic mobility". PhD thesis. University of British Columbia, 1985.

[15] J. Chu, S.C.R. Lo, and I.K. Lee. "Instability of granular soils under strain path testing". In: *Journal of Geotechnical Engineering* 119.5 (1993), pp. 874–892.

[16] R.F. Craig. *Soil mechanics*. Van Nostrand Reinhold Company, 1978.

[17] P. A. Cundall and O. D. L. Strack. "A discrete numerical model for granular assemblies". In: *Géotechnique* 29.1 (1979), pp. 47–65.

[18] Y. F. Dafalias and M. T. Manzari. "Simple plasticity sand model accounting for fabric change effects". In: *Journal of Engineering mechanics* 130.6 (2004), pp. 622–634.

[19] A. Daouadji et al. "Diffuse failure in geomaterials: Experiments, theory and modelling". In: *International Journal for Numerical and Analytical Methods in Geomechanics* 35.16 (2011), pp. 1731–1773.

[20] A. Daouadji et al. "Experimental and numerical investigation of diffuse instability in granular materials using a microstructural model under various loading paths". In: *Géotechnique* 63.5 (2013), pp. 368–381.

[21] F. Darve and O. Pal. "Liquefaction: a phenomenon specific to granular media". In: *Proceedings of the 3rd International Conference on Powders & Grains*. 1997, pp. 69–73.

[22] F. Darve et al. "Failure in geomaterials: continuous and discrete analyses". In: *Computer methods in applied mechanics and engineering* 193.27 (2004), pp. 3057–3085.

[23] H. Deresiewicz. "Stress-strain relations for a simple model of a granular medium". In: *Journal of Applied Mechanics. Transactions of ASME* (1958), pp. 402–406.

[24] R. Dobry and T. Abdoun. "An investigation into why liquefaction charts work: A necessary step toward integrating the states of art and practice". In: *Proc., 5th Int. Conf. on Earthquake Geotechnical Engineering*. Chilean Geotechnical Society Santiago, Chile. 2011, pp. 13–44.

[25] R. Dobry et al. *Prediction of pore water pressure buildup and liquefaction of sands during earthquakes by the cyclic strain method*. Tech. rep. US Department of Commerce, National Bureau of Standards, 1982.

[26] J Duffy and R.D. Mindlin. "Stress-strain relations of a granular medium". In: *Journal of Applied Mechanics. Transactions of ASME* (1957), pp. 585–595.

[27] National Research Council (US) Committee on Earthquake Engineering Research. *Liquefaction of soils during earthquakes*. National Academy of Science, 1985.

[28] Erik Eberhardt. "Rock slope stability analysis–utilization of advanced numerical techniques". In: *Earth and Ocean sciences at UBC* (2003).

[29] S.A. Galindo-Torres et al. "Strength of non-spherical particles with anisotropic geometries under triaxial and shearing loading configurations". In: *Granular Matter* 15.5 (2013), pp. 531–542.

[30] B.O. Hardin and F.E. Richart Jr. "Elastic wave velocities in granular soils". In: *Journal of Soil Mechanics and Foundations Div* 89.SM1 (1963), pp. 33–65.

[31] R. Hill. "On the elasticity and stability of perfect crystals at finite strain". In: *Mathematical Proceedings of the Cambridge Philosophical Society* 77.1 (1975), pp. 225–240.

[32] O. Hungr et al. "Rapid flow slides of coal-mine waste in British Columbia, Canada". In: *Reviews in Engineering Geology* 15 (2002), pp. 191–208.

[33] I.M. Idriss and R.W. Boulanger. "Semi-empirical procedures for evaluating liquefaction potential during earthquakes". In: *Soil Dynamics and Earthquake Engineering* 26.2 (2004), pp. 115–130.

[34] I.M. Idriss and R.W. Boulanger. *Soil liquefaction during earthquakes*. Earthquake engineering research institute, 2008.

[35] K. Iida. "The Velocity of Elastic Waves in Sand". In: 16 (1938), pp. 131–144.

[36] K. Ishihara. "Liquefaction and flow failure during earthquakes". In: *Géotechnique* 43.3 (1993), pp. 351–451.

[37] K. Ishihara, R. Verdugo, and A.A. Acacio. "Characterization of cyclic behavior of sand and post-seismic stability analyses". In: *Proc., 9th Asian Regional Conf. on Soil Mechanics and Foundation Engineering*. Vol. 2. 1991, pp. 45–68.

[38] T. Iwasaki et al. "A practical method for assessing soil liquefaction potential based on case studies at various sites in Japan". In: *Proc., 2nd Int. Conf. on Microzonation*. National Science Foundation Washington, DC. 1978, pp. 885–896.

[39] A.X. Jerves, R.Y. Kawamoto, and J.E. Andrade. "Effects of grain morphology on critical state: a computational analysis". In: *Acta Geotechnica* (2015), pp. 1–11.

[40] K.-I. Kanatani. "Distribution of directional data and fabric tensors". In: *International Journal of Engineering Science* 22.2 (1984), pp. 149–164.

[41] R. Kawamoto et al. "Level set discrete element method for three-dimensional computations with triaxial case study". In: *Journal of the Mechanics and Physics of Solids* (2016).

[42] H.D.V. Khoa et al. "Diffuse failure in geomaterials: Experiments and modelling". In: *Computers and Geotechnics* 33.1 (2006), pp. 1–14.

[43] B. Knight, C. Hichens, and J. Tozer. "BHP's deadly dam collapse linked to ramping up production". In: *ABC News* (2016). URL: http://www.abc.net.au/news/2016-02-29/bhp-samarco-dam-collapse-brazil-linked-to-ramping-up-production/7201022.

[44] S. L. Kramer. *Geotechnical earthquake engineering*. Prentice Hall Upper Saddle River, NJ, 1996.

[45] M.R. Kuhn, W.C. Sun, and Q. Wang. "Stress-induced anisotropy in granular materials: fabric, stiffness, and permeability". In: *Acta Geotechnica* 10.4 (2015), pp. 399–419.

[46] R.S. Ladd. "Specimen preparation and cyclic stability of sands". In: *Journal of the Geotechnical Engineering Division* 103.6 (1977), pp. 535–547.

[47] R.S. Ladd. "Specimen preparation and liquefaction of sands". In: *Journal of Geotechnical and Geoenvironmental Engineering* 100.10 (1974), pp. 1180–1184.

[48] P.V. Lade. "Static instability and liquefaction of loose fine sandy slopes". In: *Journal of Geotechnical Engineering* 118.1 (1992), pp. 51–71.

[49] J. S. Lee and J. C. Santamarina. "Bender elements: performance and signal interpretation". In: *Journal of Geotechnical and Geoenvironmental Engineering* 131.9 (2005), pp. 1063–1070.

[50] X. Li and X.-S. Li. "Micro-macro quantification of the internal structure of granular materials". In: *Journal of engineering mechanics* 135.7 (2009), pp. 641–656.

[51] X. S. Li and Y. Wang. "Linear representation of steady-state line for sand". In: *Journal of Geotechnical and Geoenvironmental Engineering* 124.12 (1998), pp. 1215–1217.

[52] K.W. Lim et al. "Multiscale characterization and modeling of granular materials through a computational mechanics avatar: a case study with experiment". In: *Acta Geotechnica* (2015), pp. 1–11.

[53] H. Liu and T. Qiao. "Liquefaction potential of saturated sand deposits underlying foundation of structure". In: *Proceedings of the 8th World Conference on Earthquake Engineering, San Francisco, Calif.* 1984, pp. 21–28.

[54] G. Marketos and C. O'Sullivan. "A micromechanics-based analytical method for wave propagation through a granular material". In: *Soil Dynamics and Earthquake Engineering* 45 (2013), pp. 25–34.

[55] B.W. Maurer et al. "Evaluation of the liquefaction potential index for assessing liquefaction hazard in Christchurch, New Zealand". In: *Journal of Geotechnical and Geoenvironmental Engineering* 140.7 (2014), p. 04014032.

[56] R.D. Mindlin. "Compliance of elastic bodies in contact". In: *Journal of Applied Mechanics* (1949), pp. 249–268.

[57] R.D. Mindlin and H. Deresiewicz. “Elastic spheres in contact under varying oblique forces”. In: *Journal of Applied Mechanics. Transactions of ASME* (1953), pp. 327–344.

[58] U. Mital and J.E. Andrade. “Mechanics of origin of flow liquefaction instability under proportional strain triaxial compression”. In: *Acta Geotechnica* (2016), pp. 1–11. DOI: 10.1007/s11440-015-0430-8. URL: http://link.springer.com/article/10.1007/s11440-015-0430-8/fulltext.html.

[59] U. Mital, R.Y. Kawamoto, and J.E. Andrade. “Effect of fabric on shear wave velocity in granular materials”. submitted. 2016.

[60] U. Mital, T. Mohammadnejad, and J.E. Andrade. “Flow liquefaction instability as a mechanism for lower end of liquefaction charts”. submitted. 2016.

[61] T. Mohammadnejad and J.E. Andrade. “Flow liquefaction instability prediction using finite elements”. In: *Acta Geotechnica* 10.1 (2015), pp. 83–100.

[62] J.P. Mulilis et al. “Effects of sample preparation on sand liquefaction”. In: *Journal of the Geotechnical Engineering Division* 103.2 (1977), pp. 91–108.

[63] T.T. Ng and E. Petrakis. “Small-strain response of random arrays of spheres using discrete element method”. In: *Journal of engineering mechanics* 122.3 (1996), pp. 239–244.

[64] J. O’Donovan, C. O’Sullivan, and G. Marketos. “Two-dimensional discrete element modelling of bender element tests on an idealised granular material”. In: *Granular Matter* 14.6 (2012), pp. 733–747.

[65] J. O’Donovan et al. “Analysis of bender element test interpretation using the discrete element method”. In: *Granular Matter* 17.2 (2015), pp. 197–216.

[66] A.M. Ramos, J.E. Andrade, and A. Lizcano. “Modelling diffuse instabilities in sands under drained conditions”. In: *Géotechnique* 62.6 (2012), pp. 471–478.

[67] L. Rothenburg and N.P. Kruyt. “Critical state and evolution of coordination number in simulated granular materials”. In: *International Journal of Solids and Structures* 41.21 (2004), pp. 5763–5774.

[68] I. Sanchez-Salinero, J. M. Roesset, and K. H. Stokoe II. *Analytical studies of body wave propagation and attenuation*. Tech. rep. DTIC Document, 1986.

[69] H.B. Seed. “Design problems in soil liquefaction”. In: *Journal of Geotechnical Engineering* 113.8 (1987), pp. 827–845.

[70] H.B. Seed and I.M. Idriss. *Ground motions and soil liquefaction during earthquakes*. Vol. 5. Earthquake Engineering Research Institute, 1982.

[71] H.B. Seed and I.M. Idriss. “Simplified procedure for evaluating soil liquefaction potential”. In: *Journal of Soil mechanics & Foundations Div* 97.9 (1971), pp. 1249–1273.

[72] H.B. Seed and W.H. Peacock. *Applicability of laboratory test procedures for measuring soil liquefaction characteristics under cyclic loading*. Earthquake Engineering Research Center, University of California, 1970.

[73] R.B. Seed and L.F. Harder. "SPT-based analysis of cyclic pore pressure generation and undrained residual strength". In: *Proceedings of the H. Bolton seed memorial symposium*. Vol. 2. 1990, pp. 351–376.

[74] D.J. Shirley and L.D. Hampton. "Shear-wave measurements in laboratory sediments". In: *The Journal of the Acoustical Society of America* 63.2 (1978), pp. 607–613.

[75] K.H. Stokoe, S.H.H. Lee, and D.P. Knox. "Shear moduli measurements under true triaxial stresses". In: *Advances in the art of testing soils under cyclic conditions*. ASCE. 1985, pp. 166–185.

[76] J. Thomas. "Static, cyclic and post liquefaction undrained behavior of Fraser river sand". MA thesis. University of British Columbia, 1992.

[77] X. Tu and J.E. Andrade. "Criteria for static equilibrium in particulate mechanics computations". In: *Int J. Numer. Meth. Engng* 75 (2008), pp. 1581–1606.

[78] Y.P. Vaid and J.C. Chern. "Cyclic and monotonic undrained response of saturated sands". In: *Advances in the art of testing soils under cyclic conditions*. ASCE. 1985, pp. 120–147.

[79] Y.P. Vaid and J.C. Chern. "Effect of static shear on resistance to liquefaction". In: *Soils and Foundations* 23.1 (1983), pp. 47–60.

[80] Y.P. Vaid and A. Eliadorani. "Instability and liquefaction of granular soils under undrained and partially drained states". In: *Canadian Geotechnical Journal* 35.6 (1998), pp. 1053–1062.

[81] Y.P. Vaid and S. Sivathayalan. "Fundamental factors affecting liquefaction susceptibility of sands". In: *Canadian Geotechnical Journal* 37.3 (2000), pp. 592–606.

[82] G. Viggiani and J. H. Atkinson. "Interpretation of bender element tests". In: *Géotechnique* 45.1 (1995), pp. 149–154.

[83] I. Vlahinić et al. "Towards a more accurate characterization of granular media: extracting quantitative descriptors from tomographic images". In: *Granular Matter* 16.1 (2014), pp. 9–21.

[84] R.V. Whitman. "On liquefaction". In: *Proceedings of the 11th International Conference on Soil Mechanics and Foundation Engineering, San Francisco, Calif*. 1985, pp. 12–16.

[85] D.M. Wood. *Soil behaviour and critical state soil mechanics*. Cambridge university press, 1990.

[86] J.A. Yamamuro and K.M. Covert. “Monotonic and cyclic liquefaction of very loose sands with high silt content”. In: *Journal of Geotechnical and Geoenvironmental Engineering* 127.4 (2001), pp. 314–324.

[87] S. Yamashita et al. “Interpretation of international parallel test on the measurement of Gmax using bender elements”. In: *Soils and foundations* 49.4 (2009), pp. 631–650.

[88] T.L. Youd and I.M. Idriss. “Liquefaction resistance of soils: summary report from the 1996 NCEER and 1998 NCEER/NSF workshops on evaluation of liquefaction resistance of soils”. In: *Journal of geotechnical and geoenvironmental engineering* 127.10 (2001), pp. 817–833.

[89] M. Zeghal and C. Tsigginos. “A micromechanical analysis of the effect of fabric on low-strain stiffness of granular soils”. In: *Soil Dynamics and Earthquake Engineering* 70 (2015), pp. 153–165.

Appendix A

DAFALIAS-MANZARI MODEL

Here we provide a brief description of the Dafalias-Manzari constitutive model [18] in triaxial stress space. Interested readers may refer to the original work to get a complete description. The model primarily utilizes concepts of kinematic hardening, critical state soil mechanics, and the effect of soil fabric on dilatancy; this enables it to capture both monotonic and cyclic response of soils under different loading conditions.

We denote σ_1 as the major principal effective stress, $\sigma_2 = \sigma_3$ as the minor principal effective stress, and ϵ_1, $\epsilon_2 = \epsilon_3$ the corresponding principal strains. We define pressure $p = (1/3)(\sigma_1 + 2\sigma_3)$, deviatoric stress $q = \sigma_1 - \sigma_3$, volumetric strain $\epsilon_v = \epsilon_1 + 2\epsilon_3$, and deviatoric strain $\epsilon_q = (2/3)(\epsilon_1 - \epsilon_3)$. We use superscripts e and p to denote the elastic and plastic parts of strain, respectively, and $\dot{\square}$ to denote increment in $\square$. With the notation outlined, the *i*ncremental stress-strain relations are:

$$\dot{\epsilon}_q^e = \frac{\dot{q}}{3G}; \quad \dot{\epsilon}_v^e = \frac{\dot{p}}{K} \tag{A.1}$$

$$\dot{\epsilon}_q^p = \frac{\dot{\eta}}{H}; \quad \dot{\epsilon}_v^p = \beta|\dot{\epsilon}_q^p| \tag{A.2}$$

where G is the elastic shear modulus, K is the elastic bulk modulus, H is the plastic hardening modulus associated with the increment in stress ratio $\dot{\eta}$, and β is dilatancy. Note that $\eta = q/p$ is the stress ratio. The model assumes a *h*ypo-elastic response, where the evolution of elastic moduli G and K is given by:

$$G = G_0\frac{(2.97 - e)^2}{1 + e}\sqrt{\frac{p}{p_{at}}}; \quad K = \frac{2(1 + \nu)}{3(1 - 2\nu)}G \tag{A.3}$$

where G_0 is a constant, ν is Poisson ratio, and p_{at} is the atmospheric pressure. The yield surface f is proposed to be:

$$f = |\eta - \alpha| - m = 0 \tag{A.4}$$

This defines a wedge in effective stress space, with α as the back stress, and m as a constant defining the width of the wedge such that it has an opening of $2mp$ for a given value of p. The evolution of α is governed by a kinematic hardening law:

$$\dot{\alpha} = H\dot{\epsilon}_q^p \tag{A.5}$$

where H is the hardening modulus given by:

$$H = h(M^b - \eta) \text{ with } h = \frac{G_0 h_0 (1 - c_h e)}{|\eta - \eta_{in}|} \sqrt{\frac{p_{at}}{p}} \tag{A.6}$$

where h is a positive function, M^b is the bounding stress ratio, and h_0 and c_h are scalar parameters. η_{in} is the value of η at the initiation of a loading process. To calculate $\dot{\epsilon}_v^p$, we need the dilatancy β that is given by:

$$\beta = A_d(M^d - \eta) \tag{A.7}$$

where M^d is the dilatancy stress ratio. A_d is a positive function given by:

$$A_d = A_0(1 + \langle sz \rangle) \text{ with } \dot{z} = -c_z \langle -\dot{\epsilon}_v^p \rangle (s z_{\max} + z) \tag{A.8}$$

where A_0 is a constant and $s = \pm 1$ according to $\eta = \alpha \pm m$. $\langle\rangle$ are Macaulay brackets and $z_{\max}$ is the maximum possible of state parameter z, which has an initial value of 0.

The model complies with critical state mechanics by postulating evolution laws for M^b and M^d:

$$M^b = M \exp(-n^b \psi) \text{ and } M^d = M \exp(-n^d \psi) \tag{A.9}$$

where n^b and n^d are positive constant. M is the critical state stress ratio and $\psi = e - e_c$ is the state parameter as defined by Been and Jefferies [7]. e is the current void ratio and e_c is the critical void ratio. e_c is obtained according to the relationship proposed by Li and Wang [51]:

$$e_c = e_{c0} - \lambda_c (p_c / p_{at})^{\xi} \tag{A.10}$$

where p_c is the pressure at critical state, e_{c0} is the void ratio at $p_c = 0$, and λ_c and ξ are constants.